

UNCLASSIFIED

AD NUMBER

AD837224

LIMITATION CHANGES

TO:

Approved for public release; distribution is unlimited. Document partially illegible.

FROM:

Distribution authorized to U.S. Gov't. agencies and their contractors; Critical Technology; JUL 1968. Other requests shall be referred to Air Force Weapons Laboratory, Attn: WLRP, Kirtland AFB, NM 87117. This document contains export-controlled technical data.

AUTHORITY

AFWL ltr, 30 Nov 1971

THIS PAGE IS UNCLASSIFIED

AD837224

AFWL-TR-68-33

AFWL-TR-
68-33

RESPONSE OF DISTENDED COPPER, IRON,
AND TUNGSTEN TO SHOCK LOADING

D. N. Schmidt R. K. Linde

Stanford Research Institute
Menlo Park, California

Contract NO. AF 29(601)-7236

TECHNICAL REPORT NO. AFWL-TR-68-33

July 1968

1000
AUG 8 1968

AIR FORCE WEAPONS LABORATORY
Research and Technology Division
Air Force Systems Command
Kirtland Air Force Base
New Mexico

This document is subject to special export controls and each transmittal to foreign governments or foreign nationals may be made only with prior approval of AFWL (WLRP), Kirtland AFB, NM, 87117.

AFWL-TR-68-33

RESPONSE OF DISTENDED COPPER, IRON, AND TUNGSTEN TO SHOCK LOADING

D. N. Schmidt R. K. Linde
Stanford Research Institute
Menlo Park, California
Contract AF 29(601)-7236

TECHNICAL REPORT NO. AFWL-TR-68-33

This document is subject to special export controls and each transmittal to foreign governments or foreign nationals may be made only with prior approval of AFWL (WLRP), Kirtland AFB, NMex 87117. Distribution is limited because of the technology discussed in the report.

FOREWORD

This report was prepared by the Stanford Research Institute, Menlo Park, California, under Contract AF 29(601)-7236. The research was performed under Program Element 6.16.46.01H, Project 5710, Subtask RAS1106, and was funded by the Defense Atomic Support Agency (DASA).

Inclusive dates of research were 23 June 1966 to 29 February 1968. The report was submitted 6 June 1968 by the AFWL Project Officer, Capt Joseph B. Webster III (WLRP).

Contractor's report number is SRI PGU-6127.

The authors wish to thank J. J. Dick and W. Wilkensen for their contributions to the research and their assistance in preparing this report.

This report has been reviewed and is approved.



JOSEPH B. WEBSTER III
Capt, USAF
Project Officer



HARRY F. RIZZO
Lt Colonel, USAF
Chief, Physics Branch



CLAUDE K. STAMBAUGH
Colonel, USAF
Chief, Research Division

ABSTRACT

An experimental study of the dynamic response of porous (two-thirds of crystal density) copper, iron, and tungsten was performed, using manganin and quartz transducer techniques. The data acquired include measurements of Hugoniot and release states up to about 60 kbar for porous copper, 50 kbar for porous iron, and 140 kbar for porous tungsten. It was found that inclusions in the pores substantially altered the compaction behavior of porous copper and iron, but that above about 20 kbar, "clean" foams of these materials will compact to the volumes predicted by a Mie-Grüneisen equation of state. Tungsten foam exhibited substantial residual crushing strength up to at least 140 kbar, and was thus never fully compacted under the conditions of the experiments.

Precursor amplitudes were nominally 1, 2.5, and 10 kbar for the copper, iron, and tungsten foams, respectively, and all foam materials displayed release curves similar to those for initially solid material, even when the foams were not fully compacted. Hugoniot data were obtained for solid copper and iron up to about 130 kbar, for solid tungsten up to 290 kbar, and for C-7 epoxy up to 28 kbar.

CONTENTS

<u>Section</u>		<u>Page</u>
I	INTRODUCTION	1
II	MATERIALS	3
III	EXPERIMENTAL TECHNIQUES	19
	1. Transducer Assemblies	19
	a. Manganin Wire Gages	19
	b. Quartz Gages	24
	2. Dynamic Measurement Procedures	25
	3. Electrical Recording System	28
	a. Manganin Gages	28
	b. Quartz Gages	33
IV	DATA ANALYSIS	37
V	RESULTS	43
	1. Improved Gage Calibration	43
	a. C-7 Hugoniot	43
	b. Shim Calibration	43
	2. Experimental Data for Solid and Foam Metals	45
	3. Interpretation of Results	55
	a. Temperature Effects	55
	b. Effects of Inclusions in Pores	56
	c. Release Paths	58
VI	SUMMARY AND RECOMMENDATIONS	63
	APPENDIX SUMMARY OF STATIC AND DYNAMIC DATA	65
	REFERENCES	75

ILLUSTRATIONS

<u>Figure</u>		<u>Page</u>
1	Photomicrographs of Unshocked Porous Metal Specimens (500X). (a) Iron (b) Copper (c) Tungsten	8
2	Photomicrographs of Shocked Porous Metal Specimens (500X). (a) Iron (b) Copper (c) Tungsten	9
3	Photomicrographs of Unshocked Solid Tungsten (500X). (a) Edge View (b) Top View	10
4	Longitudinal Acoustic Velocity and Density Plot for Porous Iron	12
5	Longitudinal Acoustic Velocity and Density Plot for Porous Copper	13
6	Longitudinal Acoustic Velocity and Density Plot for Porous Tungsten	14
7	Radiograph of Typical Porous Copper Specimens	15
8	Microdensitometer Records of Porous Copper Specimens (Vertical Scan)	16
9	Microdensitometer Records of Porous Copper Specimens (Horizontal Scan)	17
10	Manganin Gage Subassembly	21
11	Wire Configurations for Manganin Gages	23
12	Target Configuration Just Prior to Impact (Shown with quartz gage transducer assembly)	26
13	Projectile Assembly for Shock Attenuation Studies	27
14	Manganin Gage Recording System	29
15	Triggered Power Supply	30
16	Manganin Gage Simulator	32
17	Schematic Diagram of Acoustic Velocity Measuring System	35

ILLUSTRATIONS (Continued)

<u>Figure</u>		<u>Page</u>
18	Distance-Time Wave Interaction Diagram for Iron	39
19	Stress-Time Wave Diagram	40
20	Stress-Particle Velocity Diagram	40
21	Stress-Particle Velocity Hugoniot Curve for Armstrong C-7 Epoxy	44
22	Typical Stress-Time Profiles	47
23	Stress-Volume Hugoniot for Iron	51
24	Stress-Volume Hugoniot for Copper	52
25	Stress-Volume Hugoniot for Tungsten	53
26	Stress-Particle Velocity Hugoniot and Release Curves for Iron	60
27	Stress-Particle Velocity Hugoniot and Release Curves for Copper	61
28	Stress-Particle Velocity Hugoniot and Release Curves for Tungsten	62

TABLES

<u>Table</u>		<u>Page</u>
I	Spectrographic Analysis for Metallic Impurities	5
II	Carbon Oxidation Analysis for Organic Inclusions in Pores of Foams	6
III	Neutron Activation Analysis for Oxygen	6
IV	Data from Shock Attenuation Experiments	48
V	Densities and Acoustic Velocities on Recovered Foam Specimens	49
VI	Shot Designations Used in Figures	54
VII	Initial Conditions for Dynamic Experiments on Solid and Foam Iron	65
VIII	Precursor (Wave 1) Data from Dynamic Experiments on Solid and Foam Iron	66
IX	Shock (Wave 2) Data from Dynamic Experiment on Solid and Foam Iron	67
X	Initial Conditions for Dynamic Experiments on Solid and Foam Copper	68
XI	Precursor (Wave 1) Data from Dynamic Experiments on Solid and Foam Copper	69
XII	Shock (Wave 2) Data from Dynamic Experiments on Solid and Foam Copper	70
XIII	Initial Conditions for Dynamic Experiments on Solid and Foam Tungsten	71
XIV	Precursor (Wave 1) Data from Dynamic Experiments on Solid and Foam Tungsten	72
XV	Shock (Wave 2) Data from Dynamic Experiments on Solid and Foam Tungsten	73

SECTION I

INTRODUCTION

In work performed previously (References 1-4), distended solids (foams) were shown to be very efficient in attenuating the peak stress of a propagating shock pulse, so that a given short-duration impulse applied to one surface of a foam material could be delivered at a reduced stress level to any solid structure in contact with the opposite surface of the foam. In this manner, distended solids can serve as effective countermeasure materials in protecting a solid structure from shock damage of the sort associated with short-duration impulsive loads.

Research under these contracts has involved survey studies of representatives of several classes of porous materials, including metals, plastics, and ceramics (References 1, 2, and 3), and studies in some depth have been made on aluminum and graphite (Reference 4). All the foams studied to date have exhibited similar behavior in a general sense, but important differences in their potential effectiveness as countermeasure materials have been observed.

As part of the Air Force Weapons Laboratory (AFWL) program of vulnerability and survivability studies of possible reentry systems, an immediate need exists for Hugoniot* and shock attenuation data on foams made from metals of high atomic weight, and a long-range need exists to develop a reliable prediction capability for shock propagation and attenuation behavior in porous solids. The immediate goal of the work reported here has been to acquire the necessary data for iron, copper, and tungsten foams with densities approximately two-thirds as great as crystal density. The results of this effort should provide a

*As applied to foams in this report, the term Hugoniot means the locus of final macroscopic stress-volume or stress-particle velocity states of shocked material deduced from experimental observations with invocation of the so-called "jump" conditions (expressing conservation of mass and momentum across a shock front).

broad base of experimental data upon which to build theoretical descriptions of foam behavior and thus to satisfy the long-range needs.

We are conducting such a theoretical computational effort under Contract F29601-67-C-0073; detailed interpretations of results obtained under the present experimental program will be reserved until completion of that effort. The present report is intended to be a compilation of data obtained so far and a description of the experimental and analytical techniques used to acquire and reduce these data. Further experimental work, in addition to the theoretical computational work, will be discussed in the final report for Contract F29601-67-C-0073.

SECTION II

MATERIALS

Solid and foam iron, copper, and tungsten were supplied by AFWL for fabrication of components for quasi-static and dynamic experiments. All the flyer and driver plates were made from a solid material, which was also used for target disks in the "Hugoniot-of-solids" experiments. Foam material was used for quasi-static compression specimens and target disks for the "Hugoniot-of-foams" experiments. The solid Armco (ingot) iron and oxygen-free, low-conductivity (OFHC), solid copper samples were fabricated by AFWL. The iron, copper, and tungsten foams were manufactured by Astro-Met Associates, Inc., Cincinnati, Ohio, and the solid tungsten was manufactured by General Electric Co., Refractory Metals Division, Cleveland, Ohio.

Characterization of the metals was crucial for accurate interpretation of the dynamic results. Methods of analysis depended on the material and included both destructive and nondestructive tests. Commercially pure-grade materials were used to fabricate the copper (99.9% Cu) and Armco iron (99.7% Fe) solid specimens by normal machining and finishing techniques. All the other materials, including the "solid" tungsten which was compacted to 99.2% of crystal density by hot rolling after high-pressure sintering, were produced from graded powders (5μ to 20μ). Porous metal specimens were sintered in a dissociated ammonia (75% H_2 , 25% N) atmosphere.

Materials were used in the annealed condition with the exception of solid copper, which was approximately "1/4 hard" ("as-rolled" condition). Since copper work-hardens easily during handling, it was felt that greater uniformity and reproducibility could be obtained with material that was not fully annealed. The sintering process used in the fabrication of the foams produces annealed material, and the stress relief that occurs during the hot-rolling process used to compact the solid tungsten and process the solid iron also produces essentially annealed material. The foams were made by compacting powders at pressures

that deformed the particles and left sizable residual stresses in them. They were subsequently sintered at temperatures appropriate for their matrix materials (e.g., iron $\approx 1600^{\circ}\text{F}$, copper $\approx 1700^{\circ}\text{F}$, and tungsten $> 2000^{\circ}\text{F}$). The sintering permitted recrystallization and some metal flow and resulted in increases in strength and density of the powder compacts, while leaving individual particles in an essentially annealed condition.

Material hardness was measured on representative samples of each of the solid materials. Measured hardnesses are compared with handbook values below:

	<u>Measured Rockwell Hardness (Average)</u>	<u>Listed Handbook Value (References 5 and 6)</u>
Iron (Armco, ingot)	35B	30 to 35B = Annealed
Copper (OF)	20B	20 to 25B = 1/4 Hard
Tungsten (compacted)	40C	40C = Annealed

Special methods were required to determine the impurity content of the matrix materials and to assess the possibility of foreign inclusions in the pores of the distended metals. The impurities were classified by (1) spectrographic analysis (to test for metallic impurities), (2) neutron activation analysis (to test for oxygen impurities), and (3) carbon oxidation analysis (to test for organic inclusions in the foams). The quantitative oxygen and carbon analyses were initiated to explore the origin of apparent anomalies observed in the Hugoniot data discussed in Section V. Results of the spectrographic analysis are presented in Table I, those of the carbon analysis in Table II, and those of the neutron activation analysis for oxygen in Table III. The neutron activation analysis (performed in replicate) involved irradiating samples for 10 sec in a 14 MeV neutron flux of approximately 10^8 neutrons/cm²-sec and counting the N¹⁶-induced activity. Oxygen concentration was determined by comparing the intensity of the 6.13 MeV gamma γ photopeak of N¹⁶ from each sample with that from an oxygen standard.

Results of these analyses indicate that oxides of the metals (which are relatively dense compounds) were not present in sufficient quantities to cause

Table I
SPECTROGRAPHIC ANALYSIS FOR METALLIC IMPURITIES^a
(ppm)

Element	Tungsten			Copper		Iron	
	Foam	Solid	Solid ^b	Foam	Solid	Foam	Solid
Al	< 6
Ca	<10	...	≤ 3	100	<10	200	<10
Ag	10
Si	< 7	200	100	1300	<100
Fe	70	<50	≤13	100	50	Principal constituent	
Cr	≤ 5		
Ni	800	30	≤12	800	50	<30	100
Cu	< 3	Principal constituent		50	200
Mn	< 6			<10	1200
Mg	≤ 4	30	10	<30	250
Sn	< 6	600	100
Co	< 3	<20	20
Zr	< 3
Mo	45-65
Zn	400	200
W	Principal constituent		

^aAnalyses performed by American Spectrographic Laboratories, Inc., except as noted

^bAnalysis performed by General Electric Co. prior to sintering.

Table II
CARBON OXIDATION ANALYSIS FOR ORGANIC
INCLUSIONS IN PORES OF FOAMS

Material	Range of Carbon Content (ppm)
Iron	800 - >1000 ^a
Copper	100 - >1000
Tungsten	95 - 125

^aUp to 700 ppm of carbon may have been in the iron powders themselves.

Table III
NEUTRON ACTIVATION ANALYSIS FOR OXYGEN^a
(ppm)

Material	Oxygen Content ^b
Copper	
Foam	2600 ± 10
Solid	<100
Iron	
Foam	7000 ± 1000
Solid	550 ± 20
Tungsten	
Foam	3700 ± 100
Solid	4 ± 1

^aAnalysis performed by General Atomic Division of General Dynamics.

^bThe plus or minus values represent the range of values obtained with several different samples.

substantial filling of the foam pores. On the other hand, the iron foams and some of the copper foams contain enough carbon to suggest the possibility of significant infiltration by organic materials (which are of relatively low density, so that a small weight fraction corresponds to a substantially larger volume fraction).

Photomicrographs of porous iron, copper, and tungsten specimens are shown in Figure 1. Specimens were prepared for observation by the plastic infiltration technique described in Reference 4. Etching reagents and times were: for copper, ferric chloride, swabbed 3 to 5 sec; for iron, 3% nitric acid in alcohol, swabbed 10 sec; and for tungsten, 1 part ammonium hydroxide plus 1 part hydrogen peroxide, immersed 15 minutes. Figure 1a shows that the iron foam was composed of rounded particles with an average size of about 5μ , whereas the copper (Figure 1b) and tungsten (Figure 1c) were composed of irregular particles having an average size of about 10μ .

The postshot micrographs in Figure 2 show particle structures similar to those of preshot materials, with only small losses in particle definition. After shock, all three materials (and foam copper especially) exhibited gross plastic deformation of individual particles.

Since the solid tungsten was produced by powder metallurgy techniques, it was of interest to examine its microstructure. Figure 3 shows photomicrographs of unshocked solid tungsten specimens. The considerable grain elongation evident in Figure 3a is typical of that observed in all vertical cross-sections through the specimen thickness. Such a structure arises from the cross-rolling process used to raise the compact densities to nearly single-crystal values. Although the material had high density and compressive strength, careful handling was necessary to avoid delamination or fracture in the roll direction (along grain boundaries) during shipping and machining. Specimens were manufactured so that the direction of shock propagation would be perpendicular to the direction of grain elongation (e. g., from the top to the bottom in Figure 3a and into the plane of Figure 3b).

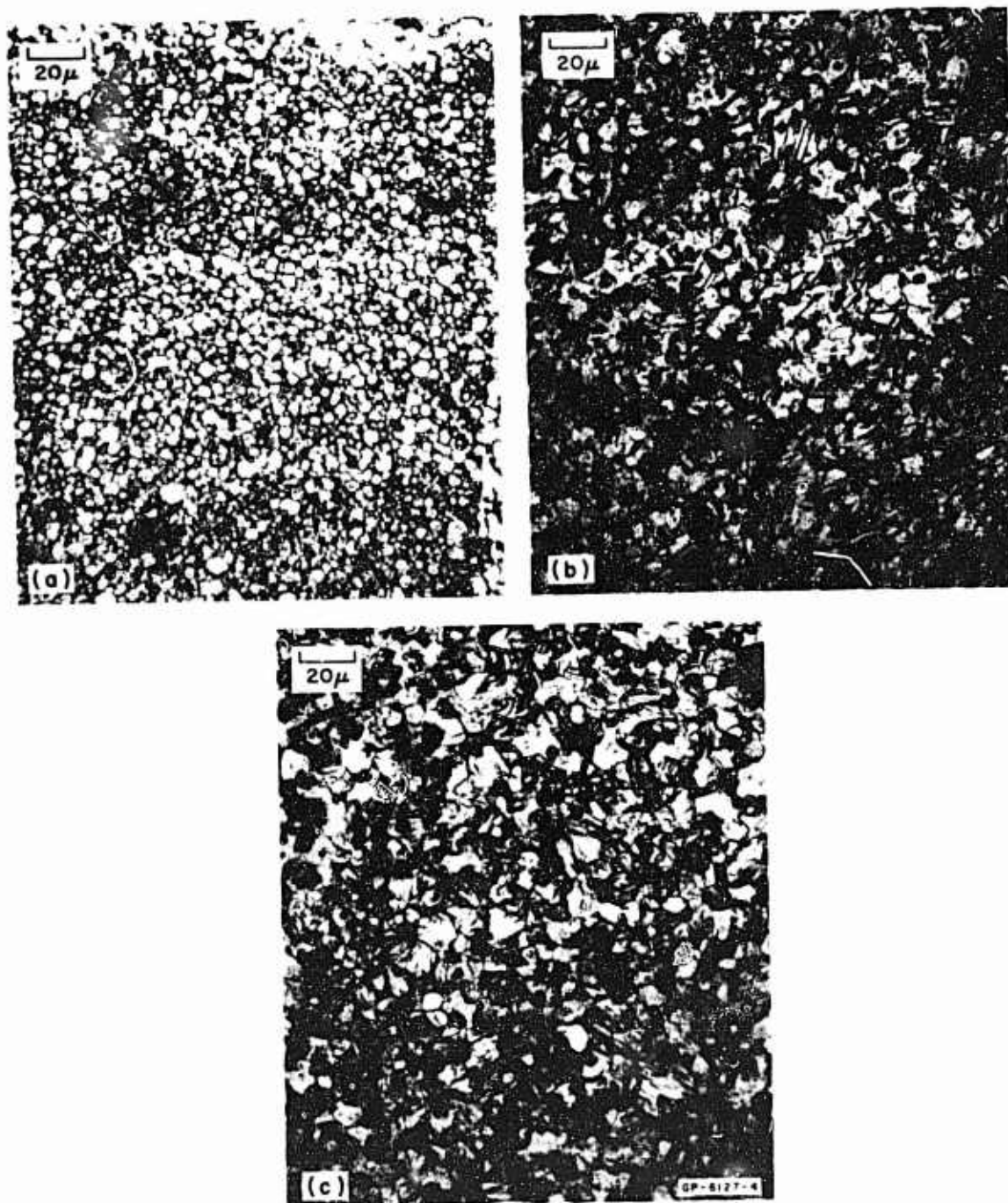


FIG. 1 PHOTOMICROGRAPHS OF UNSHOCKED POROUS METAL SPECIMENS (500X)
(a) Iron (b) Copper (c) Tungsten

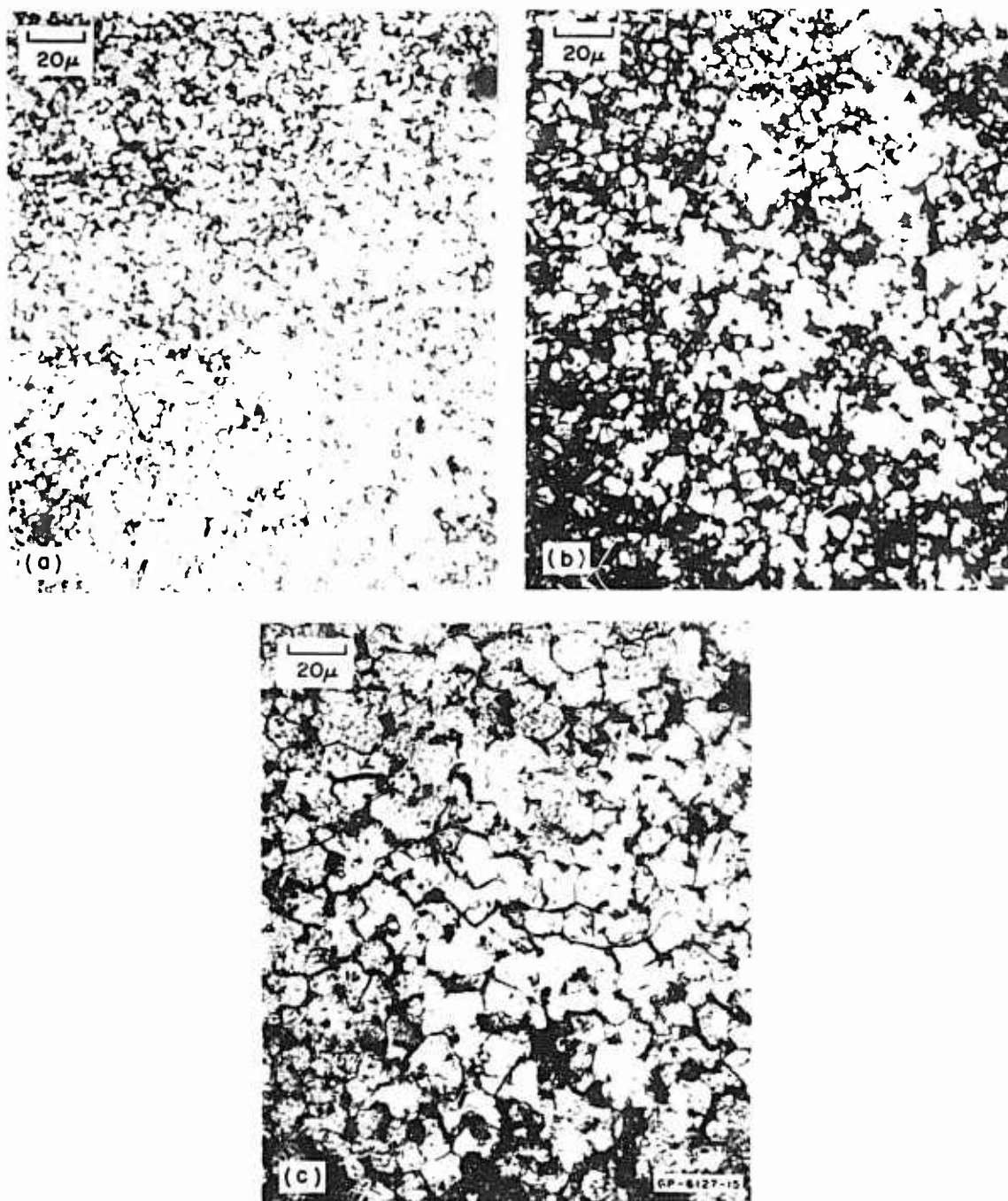


FIG. 2 PHOTOMICROGRAPHS OF SHOCKED POROUS METAL SPECIMENS (500X)
 (a) Iron (b) Copper (c) Tungsten

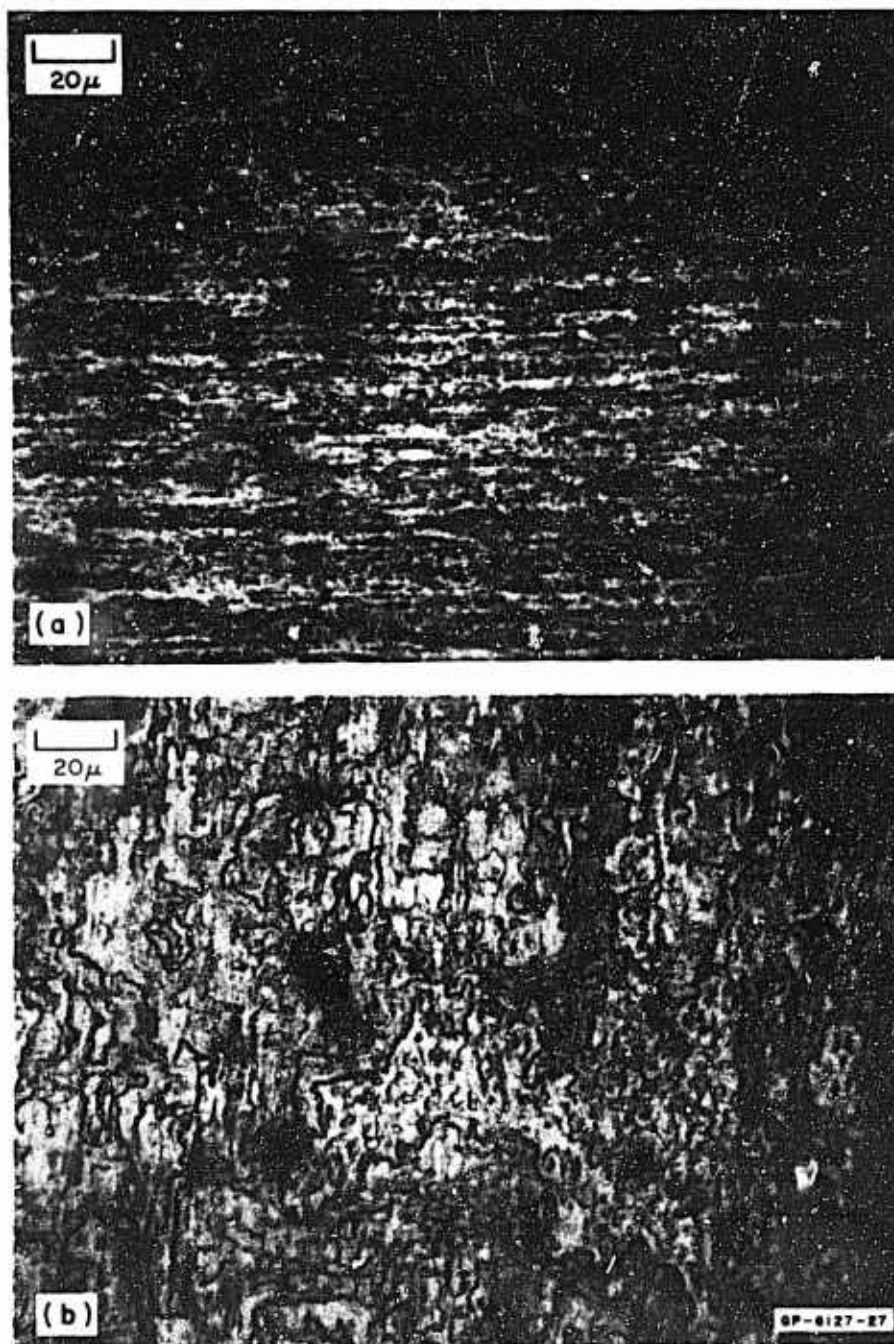


FIG. 3 PHOTOMICROGRAPHS OF UNSHOCKED SOLID TUNGSTEN (500X)
(a) Edge View (b) Top View

Densities of specimens were determined by two methods: (1) measurement of specimen weight in air and calculation of specimen volumes from measured physical dimensions, and (2) measurement of specimen weight in air and weight when suspended in a liquid. For the liquid immersion method, the foam specimens were sealed with low-density, pressure-sensitive tape and the data were adjusted for the tape volume and weight. Densities calculated by the two methods were in excellent agreement. In most cases, postshot specimens were irregular in shape (as a result of fracture), so that liquid immersion was the only practical technique for determining postshot density.

Results of density and longitudinal acoustic velocity determinations for "as-received" materials evidenced specimen-to-specimen variation in both quantities (see Figures 4, 5, and 6). Some reduction in this scatter was obtained after materials were surface-ground, cleaned in an ultrasonic cleaner, and baked in a vacuum oven (pressure $\approx 25\mu$, temperature $\approx 100^\circ\text{C}$, cycle ≈ 16 hours). Specimens used for dynamic experiments were selected from those found to cluster in the density versus longitudinal acoustic velocity ("as-received") plots in Figures 4 through 6. The effect of removing inclusions by cleaning varied among specimens, however, causing an unpredictable change in weight and longitudinal acoustic velocity. Figures 4 through 6 also present the data for all the "as-received" porous materials and for the specimen materials as they were determined after refinishing and prior to being used in experiments. It was necessary to handle these cleaned materials with extreme care, to avoid all subsequent contacts with fluids that could be absorbed, and to design the experiments in such a way that no adhesive would flow into the porous structure during construction.

Several foam specimens were individually examined by X-radiography for uniformity of density. A typical radiograph of four porous copper specimens of different thicknesses is shown in Figure 7. A solid copper stepped calibration wedge (each step 0.003 inch) is also shown. The symbols (7A, etc.) on the photograph refer to specimen numbers. If the specimen being examined is of constant thickness, the variation of optical density of the exposed X-ray film (determined with a microdensitometer) provides a measure of the actual

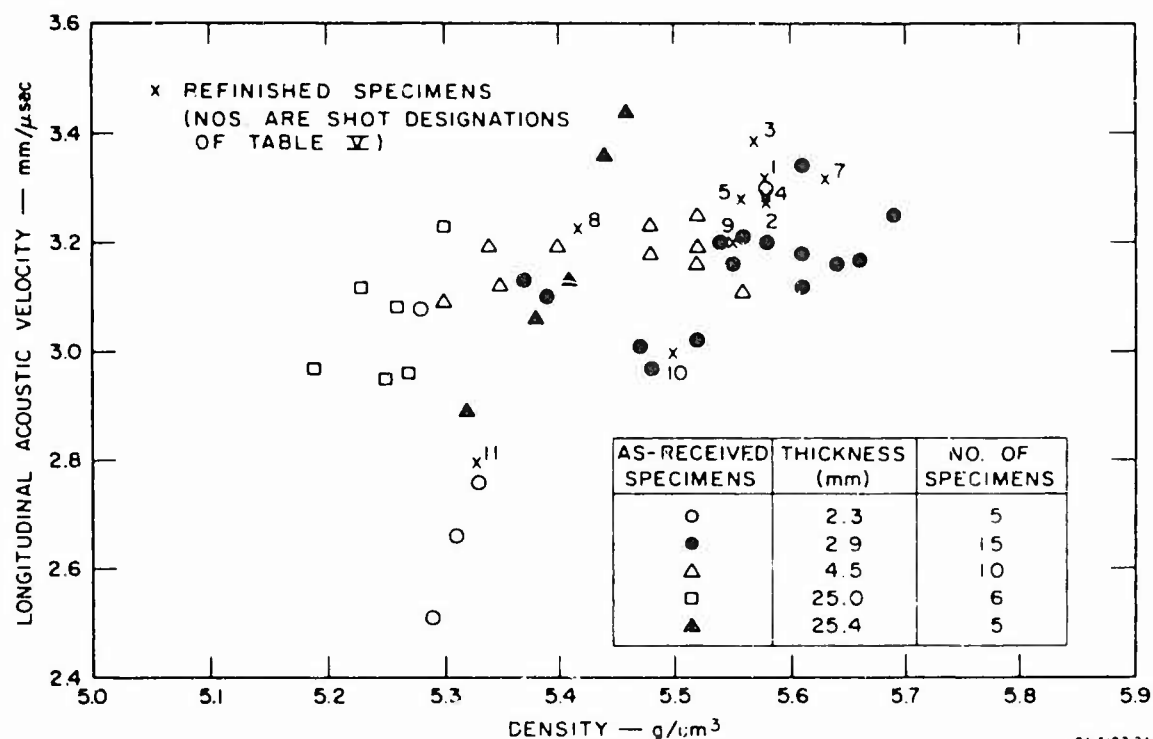


FIG. 4 LONGITUDINAL ACOUSTIC VELOCITY AND DENSITY PLOT FOR POROUS IRON

variation in specimen density. Recorded data from scanning Figure 7 in two directions are shown in Figures 8 and 9. In these figures the "scan position" is the distance from the edge of the specimen along the microdensitometer scan path, and the "equivalent solid thickness" is the solid-copper thickness which would be required to produce the same optical density of the X-ray film, as determined by the stepped calibration wedge.

The microdensitometer data indicate the existence of a radial density gradient which appears independent of scan direction and specimen. Smaller deviations (< 2% from nominal density) are measured in a central 1.5-inch-diameter zone. This is the area of major importance for the dynamic measurements. Also observed in the microdensitometer scans was a decrease in film optical density at the specimen edges. This phenomenon was observed in all the records; it arose from an X-ray beam scattering effect and should not be interpreted as a change in density.

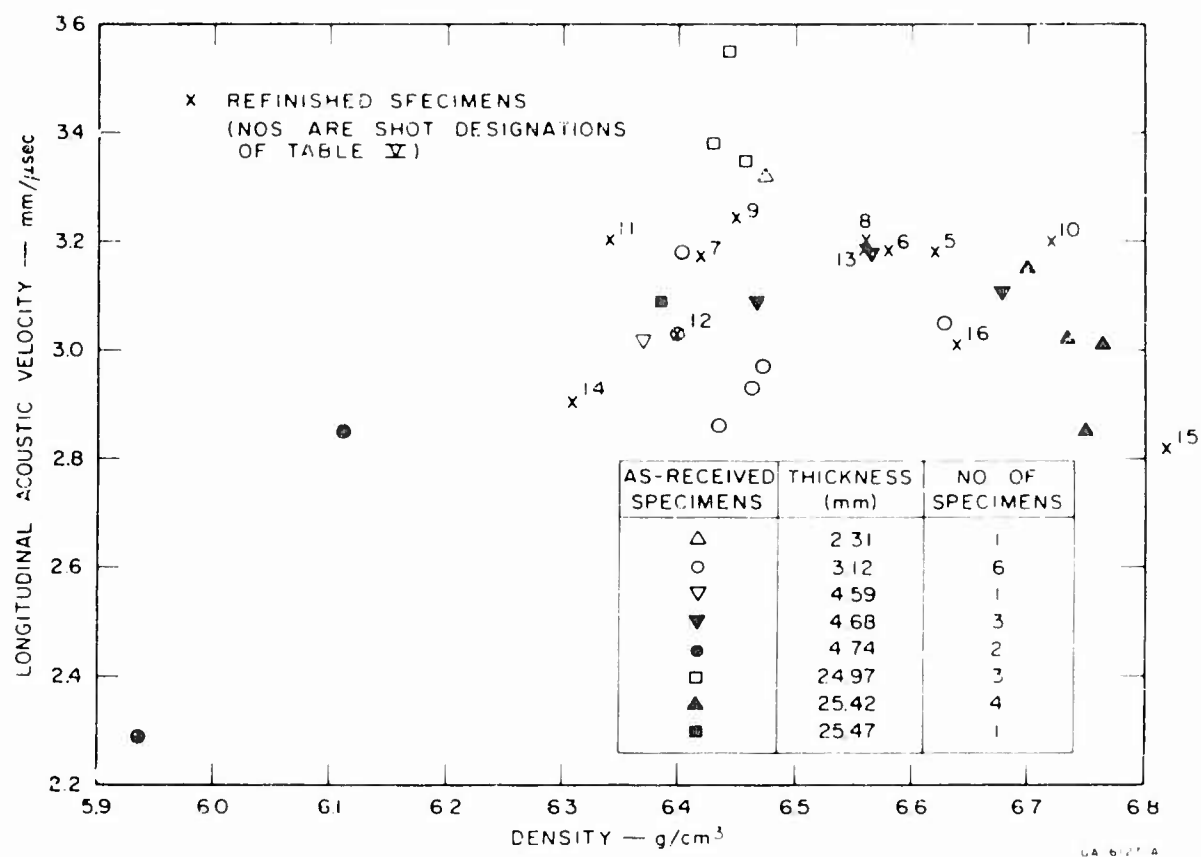


FIG 5 LONGITUDINAL ACOUSTIC VELOCITY AND DENSITY PLOT FOR POROUS COPPER

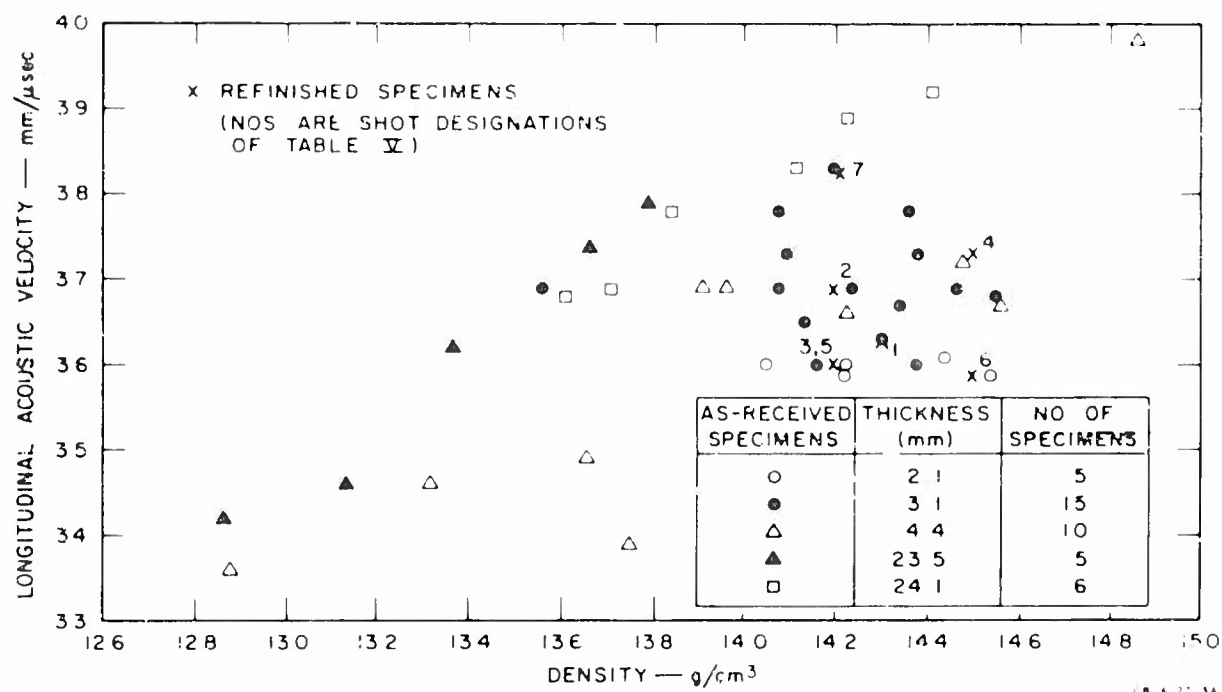


FIG 6 LONGITUDINAL ACOUSTIC VELOCITY AND DENSITY PLOT FOR POROUS TUNGSTEN

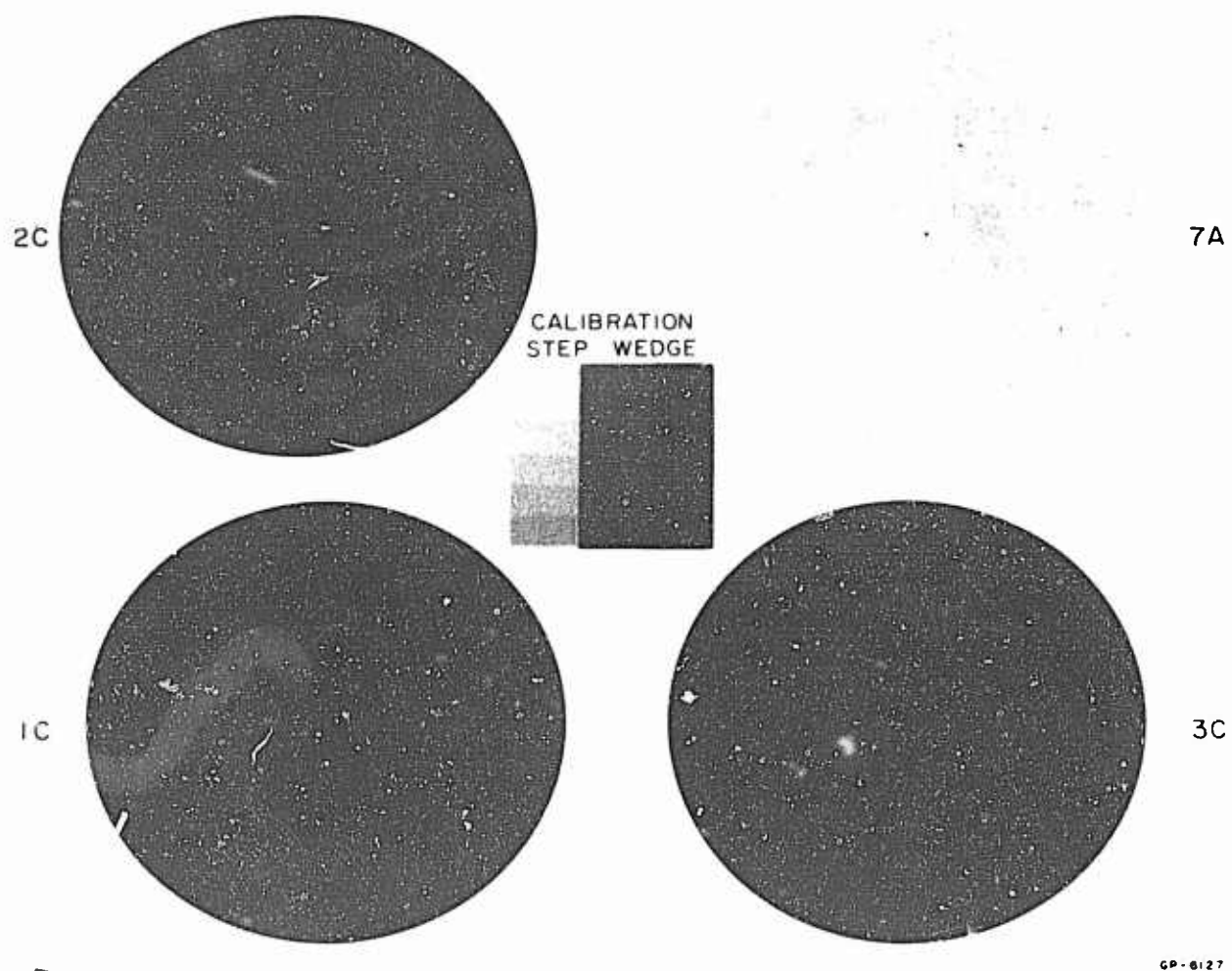


FIG 7 RADIOGRAPH OF TYPICAL POROUS COPPER SPECIMENS

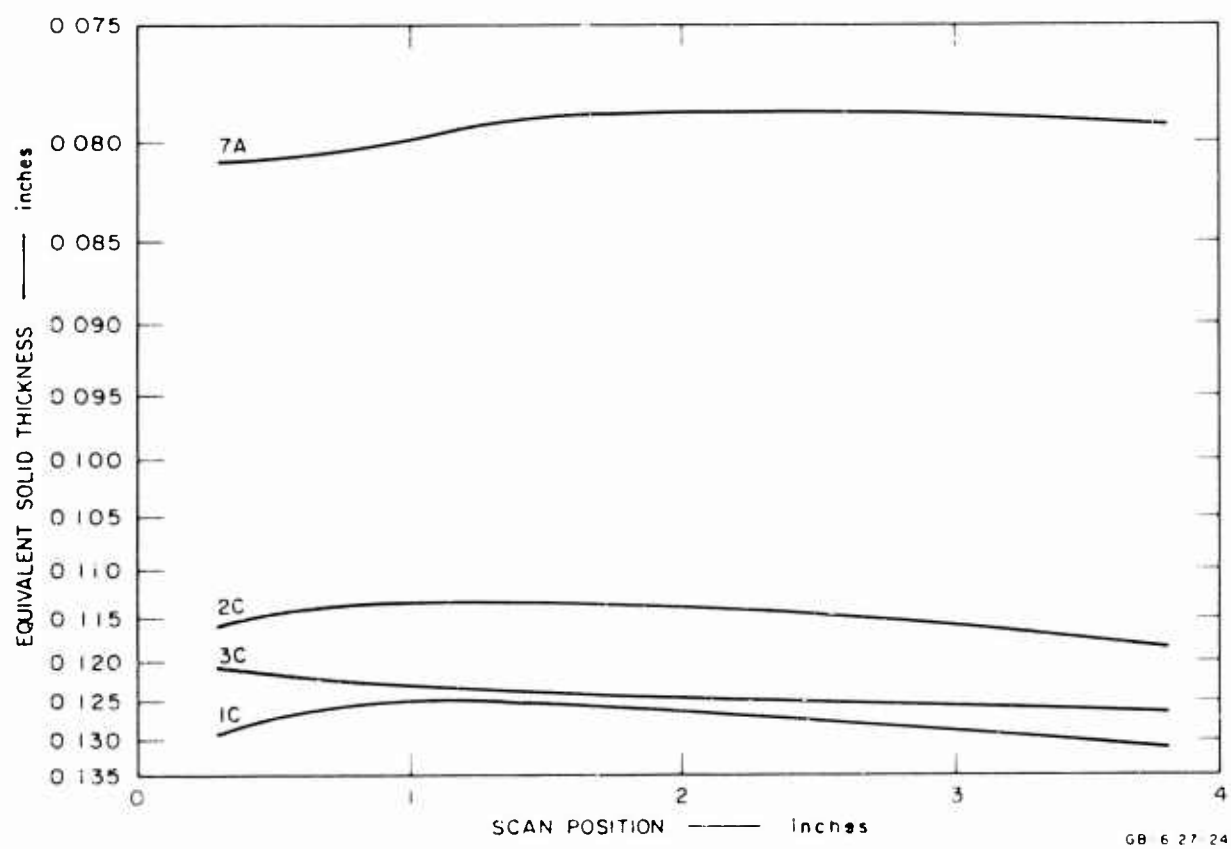


FIG. 8 MICRODENSITOMETER RECORDS OF POROUS COPPER SPECIMENS
(Vertical scan)

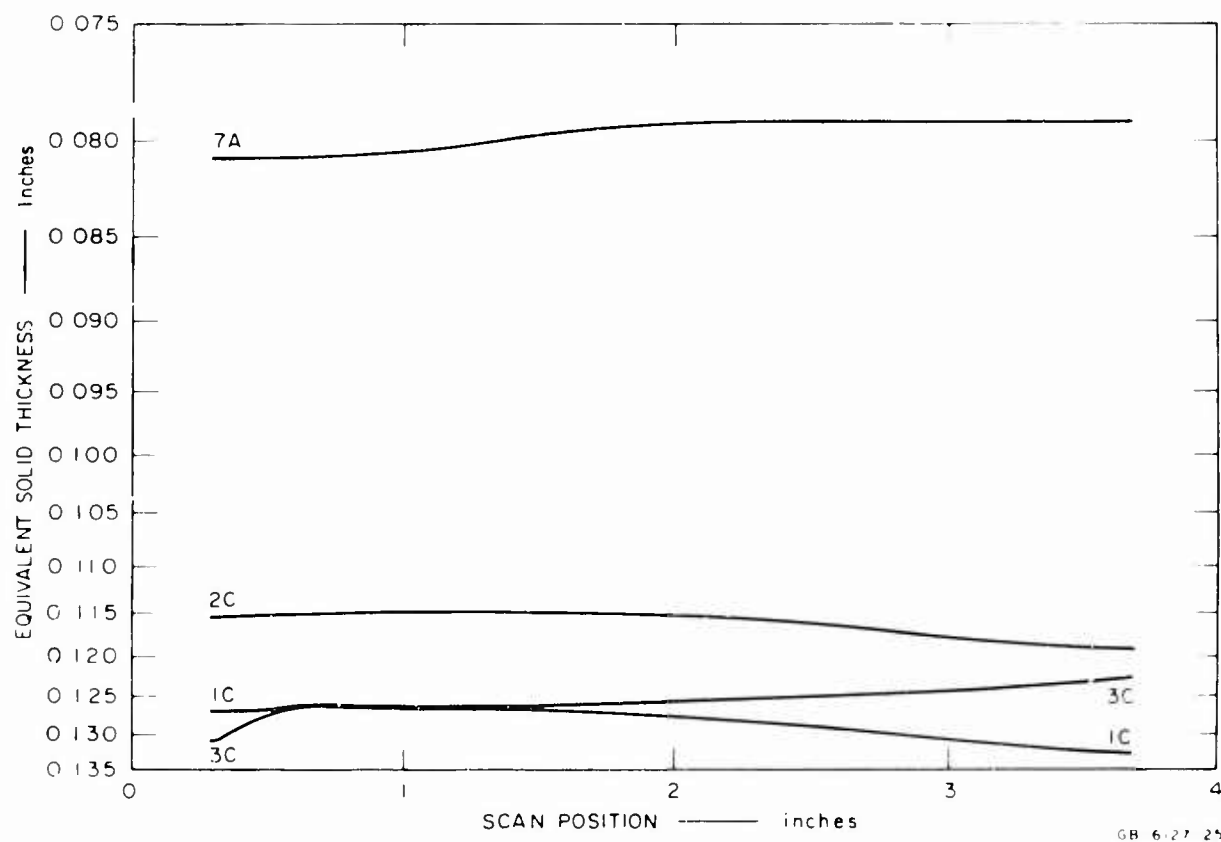


FIG. 9 MICRODENSITOMETER RECORDS OF POROUS COPPER SPECIMENS
(Horizontal Scan)

This page left intentionally blank.

SECTION III

EXPERIMENTAL TECHNIQUES

1. Transducer Assemblies

All experiments except three were conducted using either manganin wire in C-7 epoxy or quartz in glass beads transducers: in Shot 12,424 an optical free-surface measurement was observed by an image converter camera operated in the streak mode, and in Shots 12,338 and 13,116 a manganin wire in-material transducer was employed. Manganin gage fabrication procedures will be described in detail in a report being prepared under Contract F29601-68-C-0038, but it is appropriate here to discuss techniques employed in the present study.

In construction of both the manganin and the quartz gage assemblies great care was taken to ensure that all dimensions were controlled and well-measured and that shrinkage of the potting materials did not cause the gage assembly to lose contact with the sample. An air gap between the specimen and the transducer assembly would cause an error in shock transit time (as measured from the tilt pins to the gage) corresponding to the time required for the free-surface motion associated with the first wave to cause closure of the gap. As an example, it would require $0.1 \mu\text{sec}$ for the precursor wave to close a 0.001-inch gap between a typical foam iron sample and the transducer assembly. For a 0.25-inch-thick sample this would create an error of about 5% in the measured shock transit time. In many cases the precursor might not even be detected, and the arrival of the second wave would complete the gap closure.

a. Manganin Wire Gages

These assemblies consisted of two separate four-terminal 10Ω manganin gages in a cylindrical block of C-7 epoxy.* The gage elements were

*Armstrong Products, Inc., Warsaw, Indiana.

insulated from the sample by layers of epoxy of different thicknesses, corresponding to the desired shim dimensions.

Two types of C-7 epoxy castings were made in polymethylmethacrylate (Plexiglas*) forms. One was a 1-inch-long cylinder, 3.5 inches in diameter, which was drilled with two holes (1-1/8 inch in diameter) in the center parallel to the cylinder axis. This piece was used as the body of the transducer and provided electrical insulation and mechanical support for the gages. The other epoxy castings were machined and drilled as shown in Figure 10. Magnesium leads, 1/16 inch in diameter with one end filed to a 45° angle, were inserted into the drilled holes and anchored with epoxy 1/16 inch back from the front surface. The ends of these leads were tinned on the filed surface with an aluminum solder, composed of 63% Pb, 34% Sn, and 3% Zn.

A 0.002-inch-diameter manganin† wire with two voltage leads spot-welded 1 inch apart on it was soldered in place on the two magnesium current leads and the two voltage leads. The wire between the two voltage taps was formed by hand into a square grid, measuring approximately 0.25 inch on a side, as shown in Figure 10b.

A small drop of C-7 epoxy was placed over this grid and the assembly was turned over and clamped to a lapped plate covered with a 0.001-inch-thick polyester (Mylar†) sheet. After the epoxy set, the assembly was unclamped and the Mylar was removed. The thickness of the assembly from the back of the epoxy cylinder to the top of the wires (which were not completely immersed in the epoxy) was measured to ± 0.0001 inch with a micrometer. This dimension was used when grinding the epoxy to determine the separation of the gage element from the front surface of the transducer.

*Trademark of Rohm & Haas Co.

†Made by Driver Harris Co., Harrison, N.J. Nominal composition 84% Cu, 12% Mn, 4% Ni.

‡Trademark of E.I. duPont de Nemours and Company, Inc.

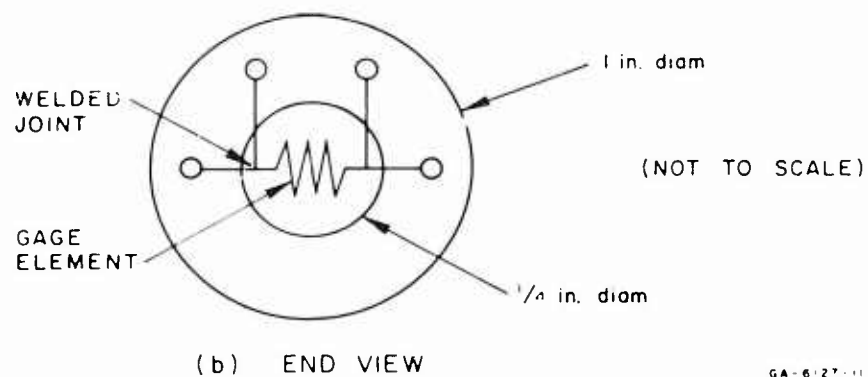
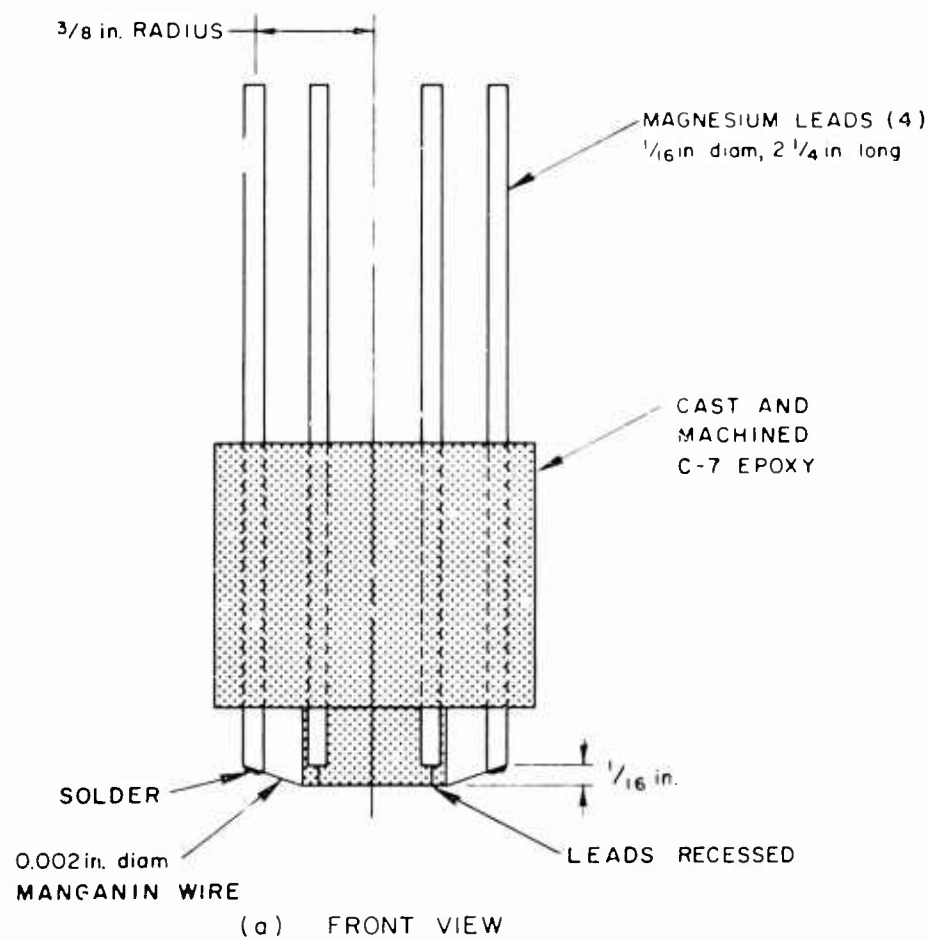


FIG 10 MANGANIN GAGE SUBASSEMBLY

GA-6127-11

Next, a layer of epoxy thicker than the desired final shim thickness was poured over the wire. After the epoxy cured, this assembly was placed in a jig perpendicular to the surface grinder table and the top was ground flat to a predetermined dimension. A photograph of two finished gages (nominally 2Ω and 10Ω) is shown in Figure 11. Two of these assemblies were epoxied into the 3.5-inch-diameter casting and the surface of the assembled pieces was finish-ground until the required planarity was produced and a measured thickness of epoxy remained in front of the wires. This completed construction of the basic manganin in C-7 gage assembly.

C-7 epoxy was used to bond the finished assembly to the sample. The transducer assembly was clamped to the sample to ensure a uniformly thin glue line, which was checked by measuring the thickness of the sample plate and the thickness of the gage prior to assembly and by comparing the total of these measurements with the finished overall thickness.

Four holes were drilled through the sample and the epoxy of the transducer assembly. Resistor ($2W\ 50\Omega$) leads were inserted in these holes and potted. These resistor leads served as the tilt pins that provided signals for measurement of impact attitude and shock velocity.

The target assembly was bonded to an adapter ring that contained the radial pins (see Reference 4). The specimen surface was measured for planarity by means of a dial indicator referenced to a granite surface plate, and the contact surface locations of the tilt pins were recorded for use in data analysis.

Coaxial cables (Type RG-58C/U) were used to connect a power supply to each gage and to monitor the voltage in the gage circuit. The resistance of each leg of the gage circuit was measured and appropriate series resistors were added to terminate the cables properly. The resistance values were also used in the data analysis (described in Reference 7) for bias corrections.

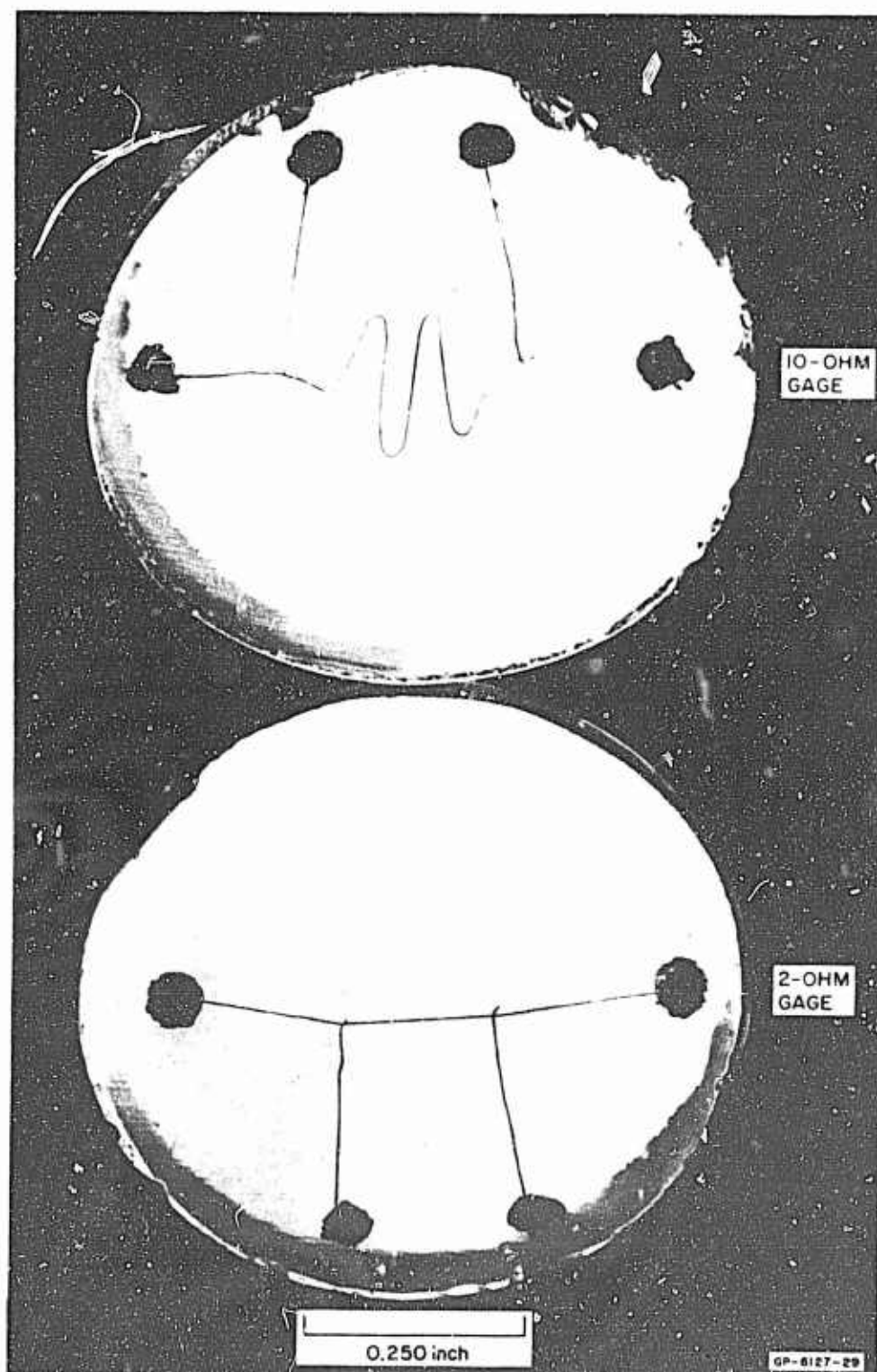


FIG. 11 WIRE CONFIGURATIONS FOR MANGANIN GAGES

b. Quartz Gages

The quartz transducer assemblies consisted of a 1.5-inch-diameter quartz gage (guard ring configuration; see Reference 8) on the surface of the sample with a shim of annealed 1060 aluminum between the foam sample and the quartz. As in the case of the manganin assemblies, the construction process was controlled so that the gage was in good contact with the sample.

A smooth circular ring, 0.500 inch in diameter and 0.003 inch wide, was cut into the conductive plating of the positive-X side of the crystal, dividing it electrically into a guard ring and a gage element. The plating was removed by a hardened steel cutting edge rotated on the gage in a lapping slurry. The edges of the quartz were lightly sanded to remove overplating and the whole gage was cleaned with ethyl alcohol before assembly.

The gage, with an aluminum shim epoxied to its front surface (≈ 0.0002 -inch glue line), was partially potted into a precast mold with a mixture of C-7 epoxy and glass beads (40 to 75μ in diameter), as described in Reference 4. The aluminum shim on the front surface of the quartz was then ground to the desired thickness and a coplanar attitude with the epoxy surface.

Electrical leads were soldered to the plated electrode surfaces of the quartz, and a 12Ω shunt resistor was attached between the grounded front surface shim and the outer electrode (guard ring) in order to maintain the center electrode (gage element) and the guard ring at essentially equal potentials during the shot. The rest of the quartz gage was then potted with the epoxy glass bead mixture to a depth slightly less than the transducer thickness. The gage assembly was epoxied to the sample and the overall thickness was measured to check for uniformity and thickness of the bond (which was generally <0.0002 inch). The tilt pins were inserted into holes drilled in the sample and epoxy, and the assembly was potted with the epoxy/glass bead mixture to a depth of at least 1.5 inches to provide mechanical support for the target assembly.

2. Dynamic Measurement Procedures

A helium-driven light gas gun (2.5-inch bore) was used to accelerate projectiles for impact with the target. The target configuration for a typical quartz transducer shot, shown in Figure 12, is similar to the arrangement discussed in detail in Reference 4. The specimen in Figure 12 is shown just prior to being impacted by the head of a projectile. On each shot, the projectile head was a full-density solid of the same composition as the matrix material of the porous target.

Impact planarity was controlled by rotating the lapped specimen surface into a position perpendicular to the axis of the gun (see Reference 4). Projectile heads were lapped in a special alignment fixture after being bonded to a projectile by a thermoplastic sheet adhesive, 0.001 inch thick. Standard aluminum projectile bodies were used on all shots.

Thin flyer plates were used in studies of shock attenuation. The projectile configuration (see Figure 13) was similar to that reported in Reference 4, but higher strength polyurethane foam was needed for physical support of the higher mass flyer plates. For each attenuation shot, the material used for fabricating the thin solid flyer plates was of the same composition as the matrix material of the porous targets.

The projectile position as a function of time was measured by using three types of pins--linear array, radial, tilt--that contacted the front surface of the projectile head as it traveled to impact with the target. The linear array pins were brass rods, 1/8 inch in diameter, with a 1/8-inch-long whisker, 0.010 inch in diameter, on the end. The whisker end of the pin projected far enough into the barrel to provide reliable contact with the passing projectile. The top linear pins (Figure 13) were connected into capacitor-discharge pulse-forming circuits whose outputs were connected to two time-interval measuring counters. These counters measured time from the first pin to the last and from the third pin to the last.

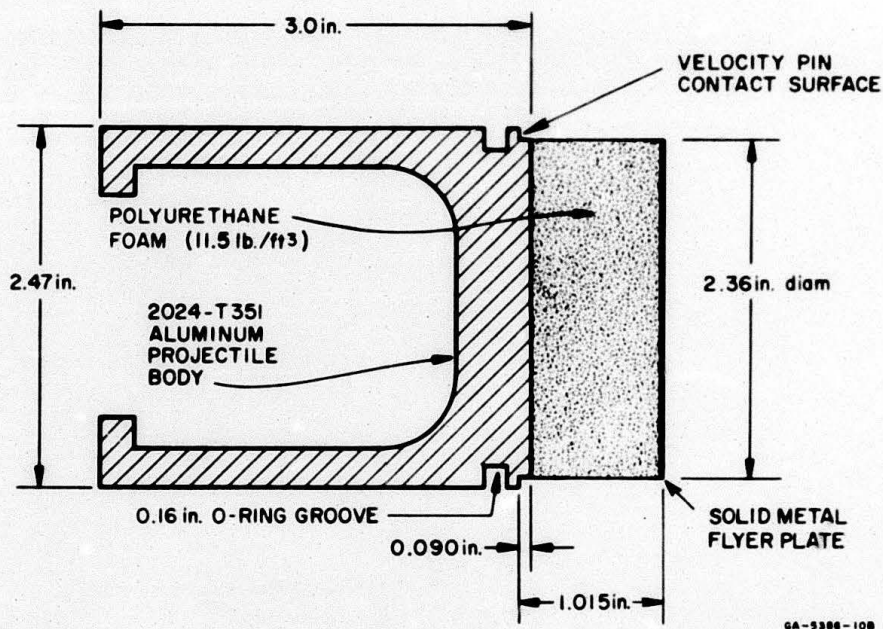


FIG. 13 PROJECTILE ASSEMBLY FOR SHOCK ATTENUATION STUDIES

As a backup system, and to correlate the velocity pin closures with the tilt and radial pin closures, the lower set of linear pins was connected through a pulse coding device to the vertical deflection plates of the cathode ray tube (CRT) of a Tektronix 535 oscilloscope with a raster-generating plug-in unit.* This unit produced sweeps of either 25 μ sec or 12.5 μ sec per line, with either 5 or 2.5 μ sec time marks. The pin closures produced coded vertical pips on the raster sweep.

At the muzzle end of the barrel, connected to the vacuum manifold, was a target-holding adapter ring, which was used to hold the specimen in the aligned position and to hold three radial pins (120° apart) in a plane parallel to the surface of the specimen and in the path of the projectile. The construction of these pins was similar to that of the velocity pins; that is, they had a 0.010-inch-diameter whisker that contacted the projectile. These pins were approximately 1/4 inch from the front surface of the target. One pin was electrically grounded to the gun

*Manufactured by Cordin Company, Salt Lake City, Utah.

barrel and had its whisker bent slightly away from the target to insure a ground potential on the projectile head during impact with the other two pins. The other two pins were connected to an amplitude-coding circuit and then to an internally triggered Tektronix 543B oscilloscope used for recording contact times.

On the surface of the target, four tilt pins were used for detecting impact time and planarity. The pins were connected to an amplitude-coding circuit similar to the radial pin circuit and then to another internally triggered, fast-sweeping ($0.1 \mu\text{sec/cm}$), Tektronix 543B oscilloscope.

The gate outputs of both the tilt and radial pin oscilloscopes were connected through a diode isolation circuit to the vertical deflection plates of the raster oscilloscope. In this way an accurate overall description of the flight of the projectile from the first linear velocity pin to the surface of the target was obtained on one record.

3. Electrical Recording System

a. Manganin Gages

The instrumentation system used to record stress-time profiles with manganin wire transducers is shown in Figure 14. Each oscilloscope display was photographed on Polaroid film, which was preserved as a record for analysis with the aid of similar photographs of the system calibration. Sweep linearity and sensitivity were tested dynamically and recorded for each shot.

Initiation of the manganin recording system occurred when the projectile contacted the radial pins. The electrical signal produced by this circuit closure was used to trigger the radial pin oscilloscope internally. The signal available from the plus gate from this instrument was directed (1) through a diode isolation circuit to the raster oscilloscope for timing data, (2) to the external trigger source for the "overall" oscilloscopes, and (3) through a programmed delay to activate a triggered power supply (see Figure 15).

The signals corresponding to resistance changes were usually on the order of tens of millivolts, while the initial turn-on step (corresponding to R_0) was on the order of one volt, so that very little resolution in ΔR was possible on the "overall" scopes. To increase the resolution, oscilloscopes with Tektronix Type W plug-in units were used. The Type W plug-in unit is a fast-rise preamp with a provision for offsetting the zero baseline to a precisely known "off-screen" level. These "offset" oscilloscopes were triggered by the plus gate output of the tilt scope through a Rutherford digital delay unit which provided the precision required by the fast-sweeping ($\approx 0.2 \mu\text{sec}/\text{cm}$) oscilloscope beams.

Timing was correlated among all the oscilloscopes by Z-axis (cathode) modulation of the oscilloscope beams, similar but not identical to the technique described in Reference 4. A Tektronix Model 105 time mark generator, set for $1.0 \mu\text{sec}$ time marks, was connected to the input of E-H Model 120D pulse generator* set for pulses 20 nsec wide, with rise and fall times of 3.5 nsec. These pulses were imposed on the Z-axes of the "radial," "tilt," and "offset" oscilloscopes and on a $0.25 \mu\text{sec}$ equivalent length of RG 58C/U coaxial cable shorted at the opposite end. This produced time marks at $0.5 \mu\text{sec}$ intervals, consisting of a blanking of the trace every $1.0 \mu\text{sec}$ and brightening of spots on the trace midway between the blanks. The bright spots helped to eliminate any ambiguity that might arise when a very long transit time was being measured in an experiment, without requiring a reduction of marker frequency.

To facilitate setting up the "offset" oscilloscopes so that the voltage level of the power supply turn-on was displayed on the cathode ray tube, a manganin gage simulator (Figure 16) was used. The simulator was inserted in the recording system in place of the manganin gage. Application of the constant current source produced an initial step followed by a resistance change approximately equal to that expected from the stress wave arrival. The arrival time of the resistance change signal could be adjusted by means of a delayed

*Manufactured by E-H Research Laboratories, Inc., Oakland, California.

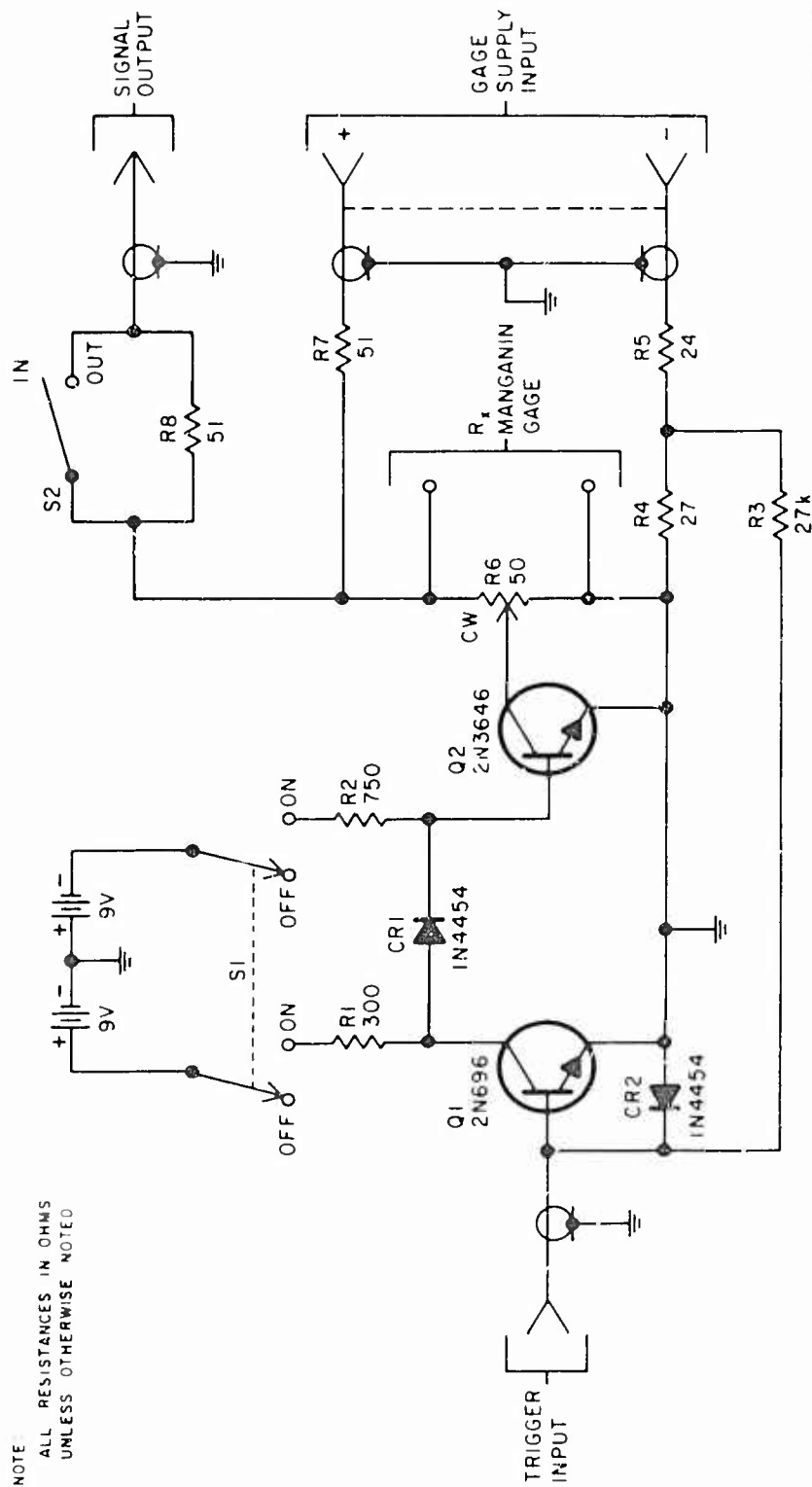


FIG. 16 MANGANIN GAGE SIMULATOR

GA 6 2' 9

trigger to correspond to the anticipated arrival of the stress wave in the actual shot.

An amplitude calibration was also necessary for "offset" beams because the wave shape had to be measured in volts and compared algebraically ($\Delta V/V$) with the offset voltage. The amplitude calibration procedure was designed to demonstrate the dynamic response of the complete recording system to stepped input pulses. The step generator consisted of a charged 2 μF capacitor discharged by means of a reed-driven, mercury-wetted relay into a 50 Ω termination. The 10% to 90% rise time of the step generator was measured to be 5 nsec.

In calibrating a particular oscilloscope and signal-line combination, the output of the generator was connected through a coaxial cable to an oscilloscope (rise time = 7 nsec), which was amplitude-calibrated with a precision ($\pm 0.1\%$) DC voltage standard. The desired maximum level of the generator was then set and displayed on the calibrated fast-rise oscilloscope while the relay was operating. The generator output was disconnected at the oscilloscope and the termination was removed from the cable, which was then connected to the signal line. On the measuring oscilloscope, a step was produced from which the rise time and attenuation of the system could be obtained. The dynamic calibration was performed after the shot had been fired, so that the calibration steps could be produced at essentially the same vertical position on the CRT as signals obtained in the actual experiment. By providing a calibration point very close to each data point, this procedure substantially eliminated errors caused by interpolation between calibration levels and by lack of vertical deflection linearity.

b. Quartz Gages

The system for instrumenting the quartz gage output was essentially the same as that for the manganin system and was similar to that described in Reference 4. The essential difference between the two types of gages is that the quartz is piezoelectric (rather than piezoresistive) and is calibrated in terms of absolute voltage output. The primary fast-sweeping oscilloscopes were triggered internally on the first rise of the pressure wave, with backup oscilloscopes

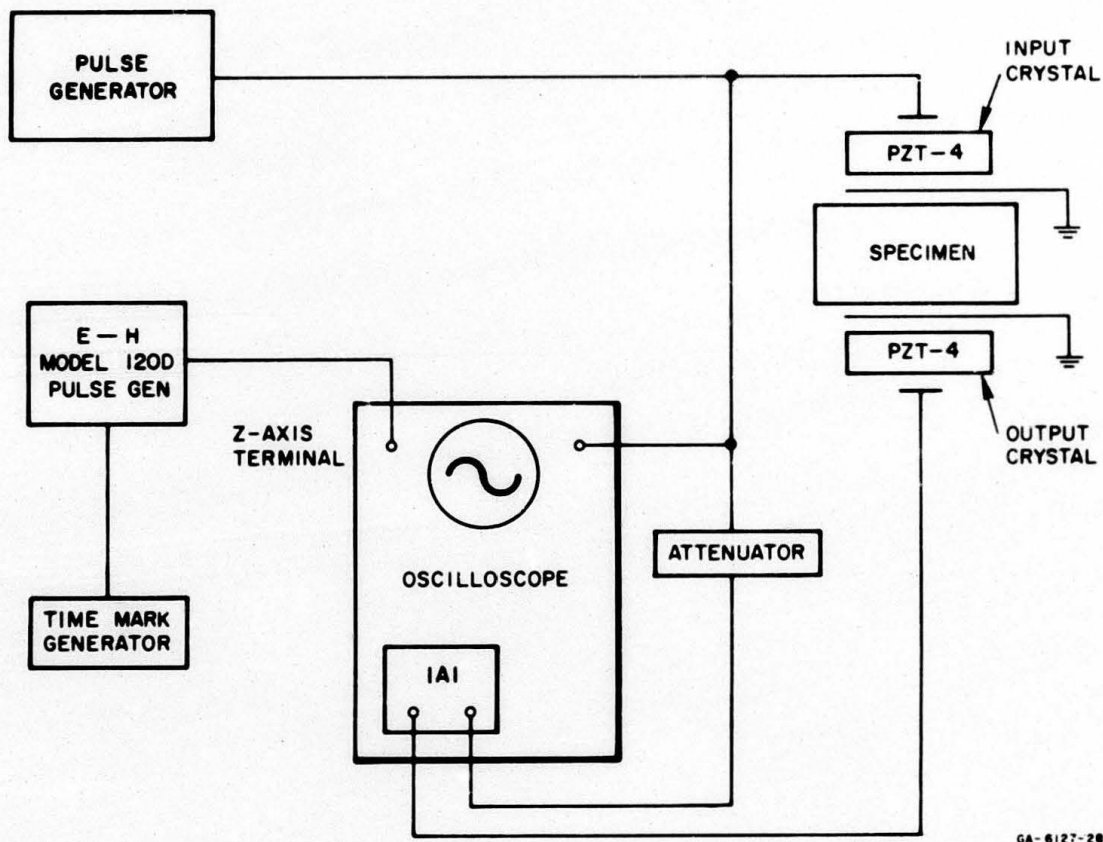
triggered from the "tilt" oscilloscope output through a programmed delay. Another oscilloscope was used to measure the output of the guard ring, which is a monitor of edge effects and wave planarity.

The postshot dynamic amplitude calibration procedure for the quartz was the same as that for the manganin system: a single calibration voltage pulse was transmitted to the measuring oscilloscope at a level corresponding to each wave amplitude or distinctive feature obtained on the actual shot record.

Longitudinal acoustic velocities were measured by a method similar, but not identical, to that reported in Reference 4. Figure 17 schematically describes the system used to measure the transit time of a short-duration mechanical pulse passed through a specimen. The propagation velocity for the disturbance was computed by dividing the specimen thickness by the measured transit time. Timing data were recorded on Polaroid film from a Tektronix oscilloscope fitted with a camera.

A 300V square-wave pulse, of about one-fourth μsec duration, from the pulse generator was converted into a small-amplitude, highly damped, sinusoidal, mechanical wave of 1 MHz frequency by a longitudinally polarized piezo-electric (PZT-4) crystal. The input crystal was held in contact with a specimen so that the surface motion would be coupled to the specimen with a uniform pre-load (≈ 200 psi). The mechanical pulse was converted back into an electrical signal after it traversed the specimen thickness by a second (output) crystal transducer.

An oscilloscope with a differential preamplifier (Tektronix Type 1A1) was used to display the electrical pulses for each of the crystals. The triggering for the oscilloscope was provided from the driving pulse of the input crystal and initiated the CRT sweep $0.1 \mu\text{sec}$ ahead of the pulse display. Amplitude attenuation was required to bring the input pulse magnitude into a range in which comparison with the output signal was possible. The preamplifier was operated in the "algebraic add" mode, which records both signals on a single sweep of the beam, eliminating errors arising from reproducibility of sweep rates.



GA-6127-28

FIG. 17 SCHEMATIC DIAGRAM OF ACOUSTIC VELOCITY MEASURING SYSTEM

Timing calibration for the acoustic measurements was provided by Z-axis (cathode) modulation from an E-H pulse generator driven by a battery-powered time mark generator. The technique was similar to the method used in the dynamic tests.

The data analysis consisted of simply locating the "first motion" point for each pulse, input and output, and determining their time separation. This separation could be estimated to within 10 nsec by interpolation between Z-axis timing marks (spaced at $0.1 \mu\text{sec}$ intervals). In the present study this produced measurements good to at least 1%, since samples had transit times $\geq 1 \mu\text{sec}$.

This page left intentionally blank.

SECTION IV

DATA ANALYSIS

1. Measurement of Hugoniot Points

Except for the "in-material" manganin gage experiments, all Hugoniot measurements were made using the impedance match method employed in Reference 4. For purposes of systematic interpretation of experimental data, shock velocities (U_1 and U_2) have been defined as the "half-wave" velocities ($1/2 U_1$ and $1/2 U_2$) discussed in Section V, and shock stresses (P_1 and P_2) have been defined as ${}_B P_1$ and ${}_B P_2$ of Section V. In the case of foams, specimens of various thicknesses were used to check that the Hugoniot results did not vary noticeably with specimen thickness.

If only a single steady-state shock is present, the impedance match analysis described in Reference 4 can provide very high precision. If a double-wave profile exists the method can still be very precise, but ideally one should employ a sensing transducer whose shock impedance is such that the precursor wave passes undisturbed through the sensing element and no reflected compressions or rarefactions are sent back into the material under study. Free-surface measurements on foams are subject to serious questions in interpretation. In-material piezoresistive gages, on the other hand, hold the greatest promise at the present time, but need further development. One shot on tungsten foam and one on copper foam were performed with 8-mil in-material gages consisting of a 2-mil manganin wire in C-7 epoxy sandwiched between two 3-mil Lucalox plates. The results of these experiments agreed well with the results from the quartz and manganin in C-7 surface gages.

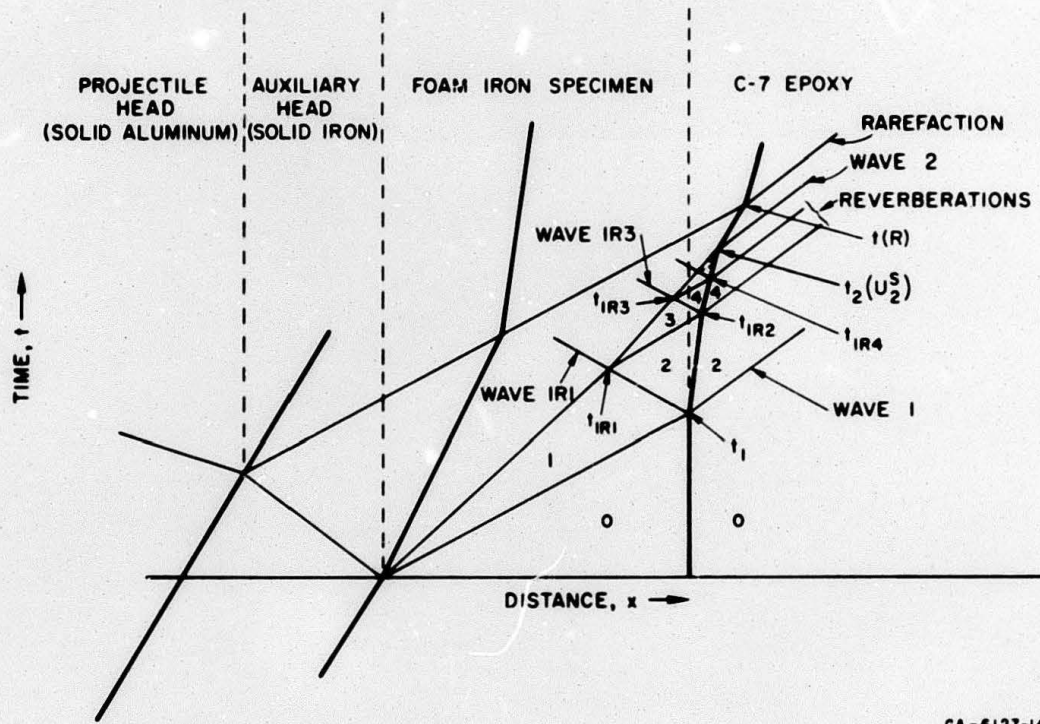
The major problem with a surface-mounted gage is that reflections of a precursor wave from the gage-specimen interface do not permit the driving wave to continue unperturbed in its passage. If the ratio of driving stress to precursor stress is large and the ratio of corresponding velocities is small,

no large errors are introduced by adopting a data reduction procedure similar to that described in Reference 4. Quartz has a shock impedance close to that of the precursor waves in the foam iron and copper of the present study; therefore, when quartz gages were used, reflections of precursors from the quartz were small.

When manganin in C-7 surface gages were used, however, it was possible and necessary to gain high precision by modifying the analysis procedure from that used in Reference 4 so as to take advantage of additional information. Reflections of precursors from C-7 were rarefactions in all cases. The analysis employed (which we have called "reverberation analysis") takes advantage of the extremely high resolution obtained in our measurements and uses the arrival of the first reverberation between gage-specimen interface and driving wave to locate the position of the driving wave at some earlier time. The x-t diagram of Figure 18 illustrates the wave interaction considered in the reverberation analysis procedure.

For a driving wave of sufficient amplitude and nonzero rise time, the reverberation of a precursor will not reflect uniformly off the entire driving wave, but primarily off some portion of the foot of the driving wave. In practice, a gage record may contain several reverberations, making it difficult to retrace the profile of the lower portion of the driving wave; in cases where this difficulty arose in the present work, profile symmetry about the "half-wave" height--i.e., symmetry about the stress $[P_1 + (P_2 - P_1)/2]$ in Figure 19--was assumed. Examination of many profiles of waves which involved only small reverberations indicated that this assumption was reasonable except when applied to very small driving waves; for such waves so much of the profile in the gage record is altered by reverberations that unperturbed rise times must be estimated from other considerations. Under these circumstances, however, a greater uncertainty is introduced by the relatively high stress and velocity ratios of the precursor to the driving wave. Hugoniot points in the very low stress regions are thus subject to greater uncertainty.

The reverberation analysis procedure, including use of the profile symmetry assumption, may be explained with reference to Figures 19 and 20,



GA-6127-14

FIG. 18 DISTANCE-TIME WAVE INTERACTION DIAGRAM FOR IRON

where the superscript G refers to the C-7 gage material in which the gage is embedded (i.e., Armstrong C-7 epoxy) and the superscript S refers to the specimen under study. From the experiment we get measurements of t_1 (the half-wave transit time for wave 1), U_1^S (the associated wave velocity), t_{1R1} (the half-wave transit time for the first reverberation), P_1^G (the first-wave pressure in C-7 epoxy), and an approximate value of U_2^S (the half-wave velocity for wave 2 in the specimen). In the laboratory coordinate system:

$$\text{Backward-facing (x decreasing)} \quad U_{1R1} = - (U_1^S - u_1^S ; U_1^S = X_1/t_1)$$

$$\text{Forward-facing (x increasing)} \quad U_{1R2} = (U_1^S + u_1^G)$$

The particle velocity, u_1^G , for state 2 is obtained from the measured P_1^S and the known C-7 Hugoniot. P_1^S and u_1^S (state 1) can then be determined by

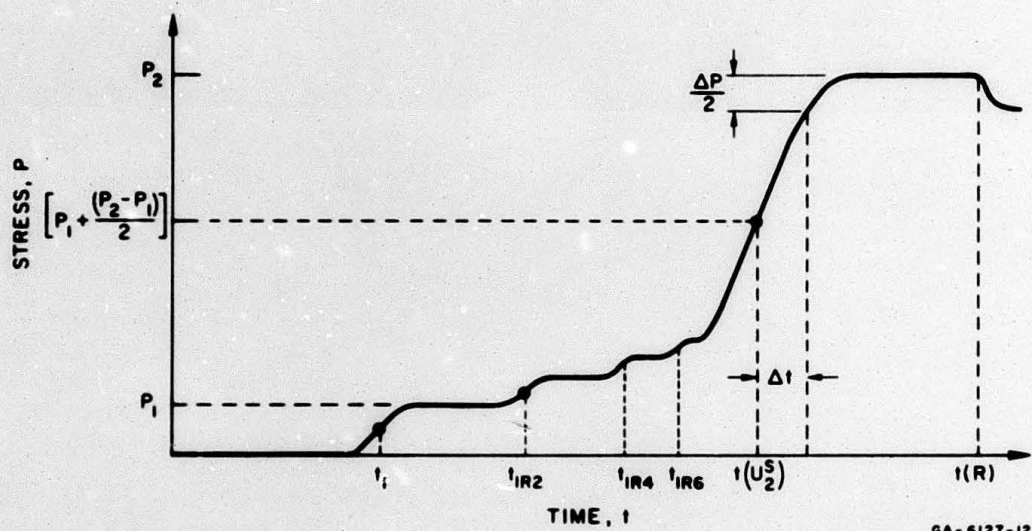


FIG. 19 STRESS-TIME WAVE DIAGRAM

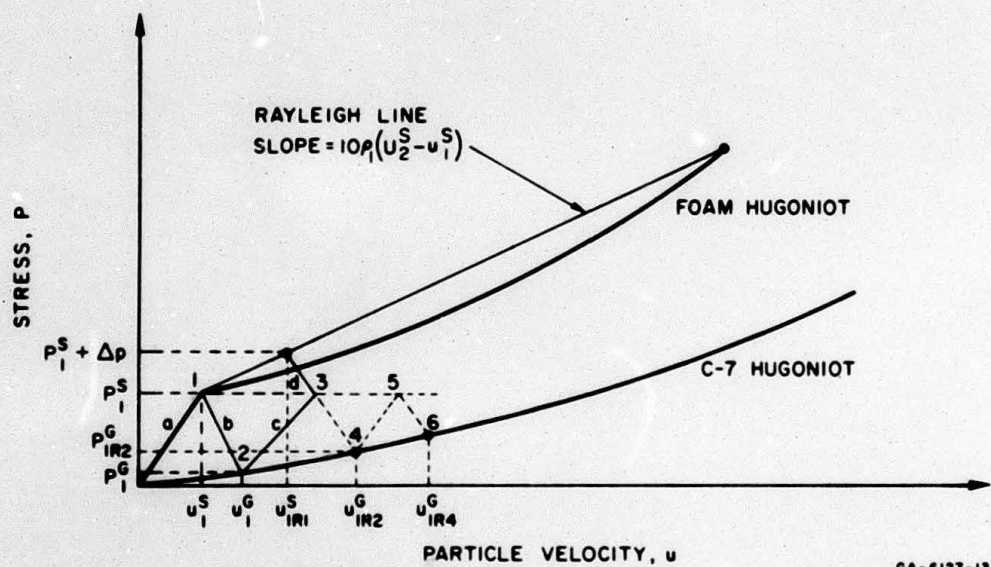


FIG. 20 STRESS-PARTICLE VELOCITY DIAGRAM

construction of lines a (connecting states 0 and 1) and b (connecting states 1 and 2) of slopes equal to $10\rho_0 U_1^S$ and $-10\rho_0 U_1^S$, respectively (see Figure 20).

Next, we draw a Rayleigh line of slope $10\rho_1(U_2^S - u_1^S)$ where the value of U_2^S is known only approximately but the resulting error has a negligible effect over the short time interval involved. Next, lines of slopes approximately $\pm 10\rho_0 U_1^S$ are drawn from state 3. This determines Δp (Figure 20), an estimate of the pressure increment at the foot of the second wave which participates in sending off a new elastic wave 1R2 after the reverberation interaction between wave 1R1 and wave 2. Since wave 2 has finite rise time, the half-wave velocity, U_2^S , equals $X_2/(t_{1R1} + \Delta t)$, where Δt is the time interval from $[P_1 + (P_2 - P_1)/2]$ to $(P_2 - \Delta p)/2$ on a straightline approximation* of the wave 2 profile. This assumes that the wave profile measured at $t(U_2)$ from $[P_1 + (P_2 - P_1)/2]$ to P_1 is symmetric with the wave profile from $[P_1$ to $P_1 + (P_2 - P_1)/2]$ before time t_{1R1} .

Then an "exact" Rayleigh line for wave 2 can be calculated with a slope equal to $\{[10\rho_1 x_2/(t_{1R1} + \Delta t)] - u_1\}$. This, with the known projectile Hugoniot, determines the state of the foam (P_2^S, U_2^S) that would result from the passage of the undisturbed double shock wave.

*This approximation is used when $P_2 \gg P_1$, in order to eliminate errors associated with the 90%-100% portion of the rise time for the electronics response. In such cases (i.e., when $P_2 \gg P_1$), the error in calculated Hugoniot state resulting from this straight-line approximation will be small.

This page left intentionally blank.

SECTION V

RESULTS

1. Improved Gage Calibration

Increased knowledge of manganin and quartz gage response resulted as a by-product of this study.

a. C-7 Hugoniot

Figure 21 shows an "improved" low-pressure Hugoniot for Armstrong C-7 epoxy obtained from the results of the solid copper, iron, and tungsten Hugoniot shots and assumed elastic-plastic release curves. Any uncertainties in the calibration factor for the manganin gage are built into this improved Hugoniot, so that it is well-suited for use in reducing data from manganin gage shots. Data from Reference 7 are included on the figure for comparison and extrapolation purposes.

If the stress P is given in kilobars and the particle velocity u is given in mm/ μ sec, a least-squares fit to the combined data up to 80 kbar yields the equation for the Hugoniot of C-7 epoxy:

$$P = 19.19 u^2 + 30.47 u \quad (1)$$

This Hugoniot has been used in Figure 21.

b. Shim Calibration

The effects of various thicknesses of nonelastic shims were evaluated in experiments on porous materials on quartz and manganin transducers. The need for such data was established in earlier work with quartz transducers in which abnormally low voltage outputs were obtained when the stress was

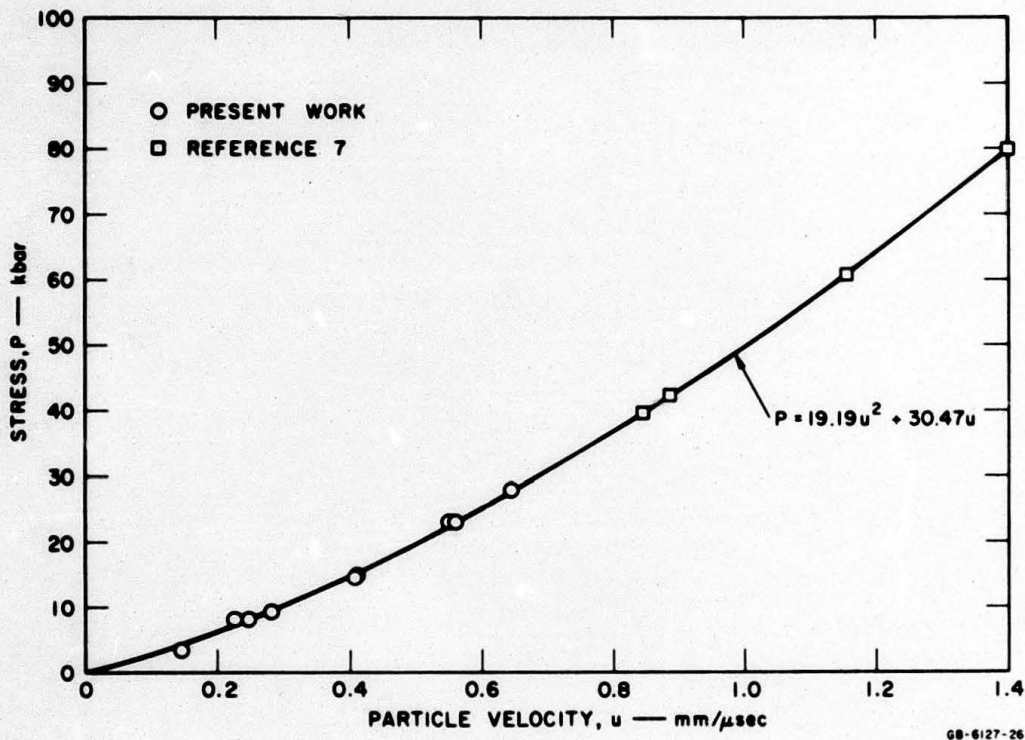


FIG. 21 STRESS-PARTICLE VELOCITY HUGONIOT CURVE FOR ARMSTRONG C-7 EPOXY

transmitted directly to the quartz from a porous material (Reference 4). It was argued that this behavior of quartz might be rationalized on the basis of the piezoelectric response of the quartz to a nonplanar, nonuniform strain. Since the foam transmits to the quartz a stress profile that is initially "rippled" along the foam-quartz contact surface, it was argued that the wave front varies locally in three dimensions as it propagates into the quartz, and since the quartz responds elastically at the stress levels in question, a three-dimensional pattern of local variations is maintained within the quartz. The piezoelectric coefficients for quartz are such that one might expect such a stress field to cause the current from the positive-X face of the quartz to be less than that obtained when the gage is calibrated against solid materials. The same effect has been observed when the foam material is replaced by a carbon-phenolic composite material, which is solid rather than porous but is inhomogeneous on roughly the same scale as the foams used in Reference 4. In the case of manganin piezoresistive gages,

nonlinear stretching of the wire might occur if no buffer were present. In either case, any effects on the gages should depend on the particle size of the foam constituents as well as on their particle shape and the degree of porosity.

Two shots employing iron foam specimens were fired to determine the effect of shims on measured peak stress. For the first shot, five manganin gages built on a 0.001-inch-thick Mylar insulator were used. One gage was placed directly in contact with the iron foam sample. Annealed aluminum shims, 0.012, 0.032, 0.040, and 0.125 inch thick, were used under the other gages. In the second shot various thicknesses of C-7 epoxy--0.002, 0.012, 0.031, and 0.040 inch--were substituted for the Mylar insulator and aluminum.

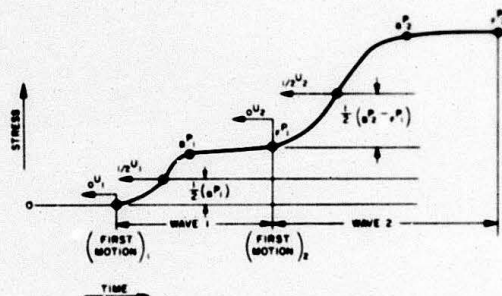
Although erratic readings were obtained when the gages were placed close to a foam surface, results from the C-7 epoxy shim shots indicate that an epoxy thickness of 0.012 inch is adequate for the conditions of the present study. The pressure measured by the manganin gages as a function of aluminum thickness was, within experimental error, independent of shim thickness.

Shims of annealed aluminum were investigated for use with standard quartz gages (3/8 inch thick) and quartz arrival transducers (0.050 inch thick). A shot was fired using shims 0.003, 0.010, 0.019, 0.030, and 0.125 inch thick. The recorded pressures for waves 1 and 2 were compared with results from gages that had no shim. Recorded pressures in the latter gages were lower by more than 10%. The 0.010-inch shim appeared to be sufficiently thick to provide reliable stress readings for the specific foams employed in the present study.

2. Experimental Data for Solid and Foam Metals

Measured and calculated data from all shots fired are tabulated in the appendix. The duration of the flat-topped input shock pulse was determined in each experiment by the material and thickness of the projectile head. The shock pulses employed to establish Hugoniot points were of sufficient duration to ensure that no erosion of the peak stress level could occur during transit of the shock through the specimen.

Shock-wave profiles are described by the notation represented on the schematic stress-time profile shown below:



These symbols are discussed in Reference 4. Figure 22 is a collection of actual profiles observed in experiments on the materials under study. The multiple wave structure visible in the examples shown includes reverberations of the precursor (wave 1) between the specimen-transducer interface and the driving wave (wave 2). Some profiles also evidence a step relief of the peak stress for wave 2. This is caused by the arrival of rarefactions from the interface between the projectile head and the aluminum projectile body (Figure 12).

Shock attenuation experiments were performed on each of the foam materials. Unfortunately, the angles of impact (tilt) were larger than desired. This experimental problem has been solved, and further experiments are currently being pursued under Contract No. F29601-67-C-0073. A brief summary of these shots is given in Table IV.

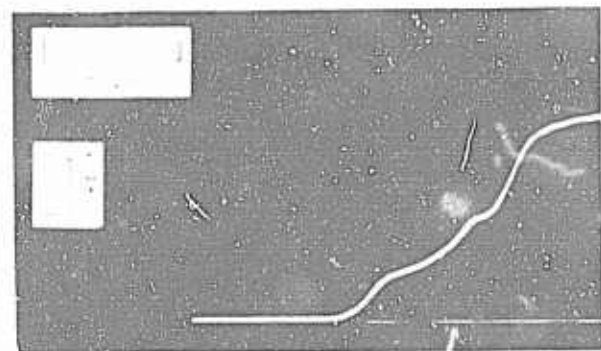
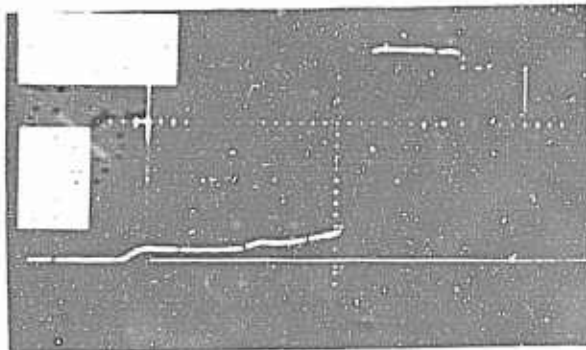
Experimental data and results of Hugoniot and release curve computations for solid and porous iron, copper, and tungsten are presented in the appendix. The characteristics of the specimen prior to impact and the projectile velocity are included, as are measured and calculated data for waves 1 and 2.

Measured densities and longitudinal acoustic velocities of foam specimens recovered after shocking are listed in Table V for all cases in which suitable specimens were collected and identified from postshot remains. Initial density,

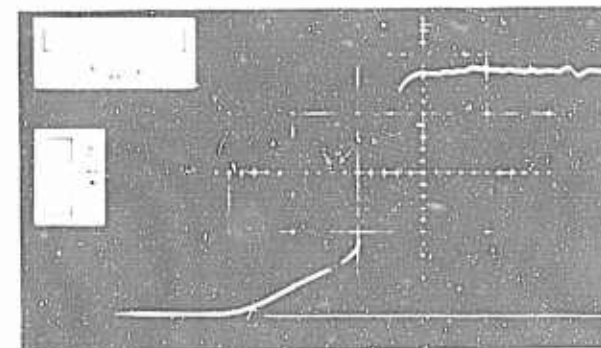
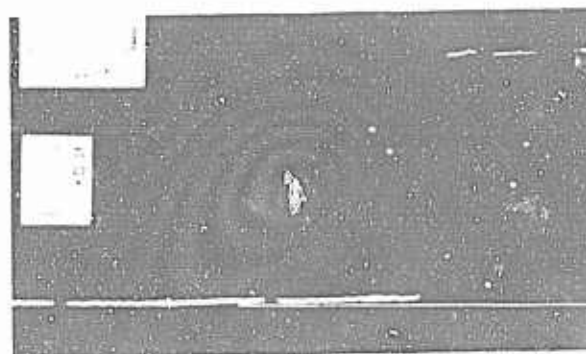
FOAM

SOLID

IRON



COPPER



TUNGSTEN

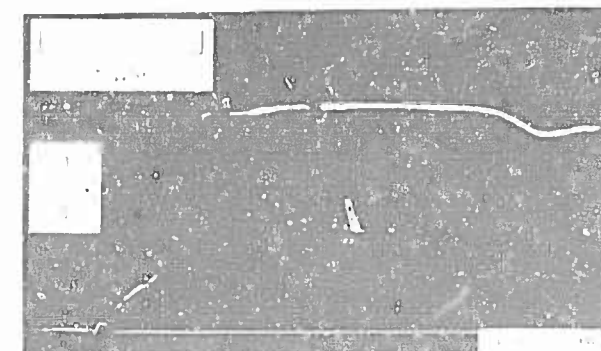
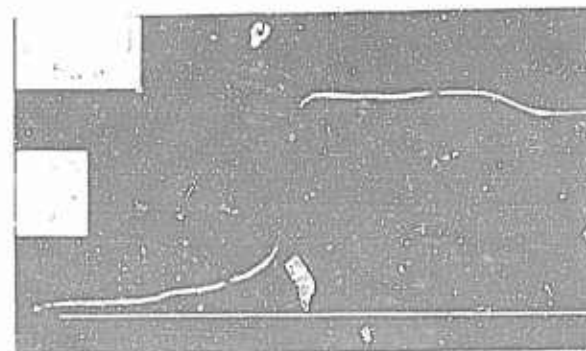


FIG. 1. TYPICAL STRESS TIME PROFILES

Table IV

DATA FROM SHOCK ATTENUATION EXPERIMENTS

Shot No.	Description of Specimen				Impact Conditions		Transducer Type
	Material	Density (g/cm ³)	Thickness (mm)	Projectile Velocity (mm/ μ sec)	Input Momentum Density ^a (dyne-sec/cm ²) $\times 10^4$	Shock Tilt across Gage (μ sec)	
12992	Copper	6.70	1.9	0.65	3.0	0.18	Quartz ^b
12997		6.00	4.18	0.88	3.9	0.16	
12990	Iron	5.50	4.27	0.76	2.6	~0.2	Quartz
12993		5.33	2.17	0.64	2.7	>0.2	
13004	Tungsten	14.44	2.15	0.67	6.4	0.016	Manganin
13012		14.51	2.15	0.67	6.4	0.029	

^a Using a solid flyer plate ≈ 0.020 -inch thick.

^b 0.010-inch-thick annealed 2024 aluminum shim used between foam and quartz gage.

Table V

DENSITIES AND ACOUSTIC VELOCITIES OF RECOVERED FOAM SPECIMENS

Shot No.	Density ρ_o (g/cm ³)	Initial Longitudinal Acoustic Velocity (mm/ μ sec)	Estimated Peak Stress P_{max} (kbar)	Final Density ρ_r (g/cm ³)	Final Longitudinal Acoustic Velocity (mm/ μ sec)
Iron					
(Solid)	(7.81)	(5.96)
12646	5.58	3.32	50	7.1	4.5
12662	5.57	3.28	24	7.1	---
12671	5.58	3.29	16 ^a	7.2	4.4
12672	5.56	3.28	9 ^a	6.9	4.5
13128	5.50	3.3	24 ^a	7.9	4.1
13130	5.33	2.8	46	7.5	4.1
Copper					
(Solid)	(8.94)	(4.98)
12567	6.62	3.18	37	8.5	4.7
12568	6.58	3.18	54	8.5	---
12571	6.56	3.20	50	8.5	---
12574	6.45	3.24	9 ^a	8.4	4.6
12644	6.72	3.20	10 ^a	8.5	4.7
12645	6.34	3.20	22 ^a	8.5	4.8
13056	6.31	2.9	37 ^a	8.4	3.4
13057	6.82	2.8	21 ^a	7.7	3.2
13058	6.64	3.0	7 ^a	6.4	4.0
Tungsten					
(Solid)	(19.2)	(5.4)
12994	14.3	3.63	107	18.8 \pm 0.2	4.8
12995	14.2	3.69	139	18.6 \pm 0.5	4.5
13000	14.2	20.2 \pm 0.4	3.6
13050	14.4	3.73	32	16.5 \pm 0.1	4.0
13052	14.1	20.2	3.9
13059	14.5	3.59	82	15.0 \pm 0.4	4.5

^a P_{max} corresponds to reflected shock produced at foam-quartz interface

ρ_0 , and final density, ρ_f , were computed from weight-volume measurements and from liquid immersion measurements. An estimate of the peak stress, P_{\max} , experienced by the foam, accounting for the effects of reflected shocks, is also included.

Hugoniot data are plotted in the P-V plane for each material in Figures 23 through 25. The shot designations used in the figures are identified in Table VI. These plots contain results from dynamic experiments on solid and foam material, as well as "static" measurements of initial volumes and of postshock volumes, where possible. Initial foam volumes are scattered over several percent and represent the specimen-to-specimen variations of the original sample material. These data are plotted along the zero stress coordinate and should be associated with the numbered Hugoniot elastic limit (HEL) points to which they are attached. These numbers designate data points associated with the same shot (e.g., HEL, final Hugoniot state, and postshock state for a given specimen).

Hugoniot data for the solid materials from the literature (References 9, 10, and 11) and from the current experimental effort are included in the figures. Results from the present work are in good agreement with the copper data of Reference 10 in the range from 20 to 60 kbar. Prior to the present study, no data for solid tungsten at stresses below 400 kbar had been reported. However, the present data, which extend to about 300 kbar, extrapolate smoothly into the data of Reference 11. The published data on Armco iron in the 20 to 60 kbar range (Reference 9), however, display a systematic offset in relative volume of up to 0.4% from the results obtained in the present work.

The porous metals exhibit scatter of several percent in initial volume, precursor amplitudes, and precursor velocities for each material. It is noteworthy, however, that within the limits of scatter, the propagation velocity of the first detectable signal ($_0U_1$) in a shock experiment on these materials is roughly equal to the measured longitudinal acoustic velocity.

In the case of final Hugoniot states for the foams, it is clear that most of the data do not lie close to the Hugoniots of the respective solids. This result

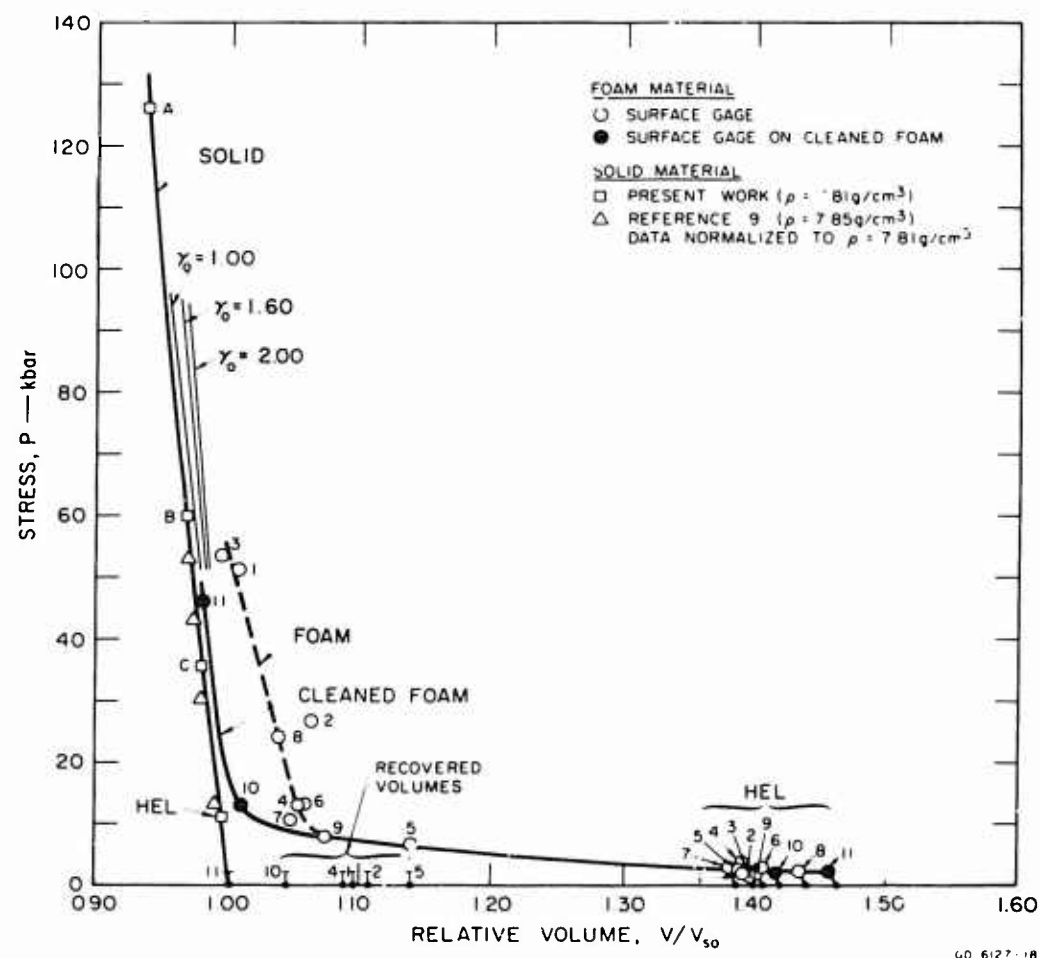


FIG. 23 STRESS-VOLUME HUGONIOT FOR IRON

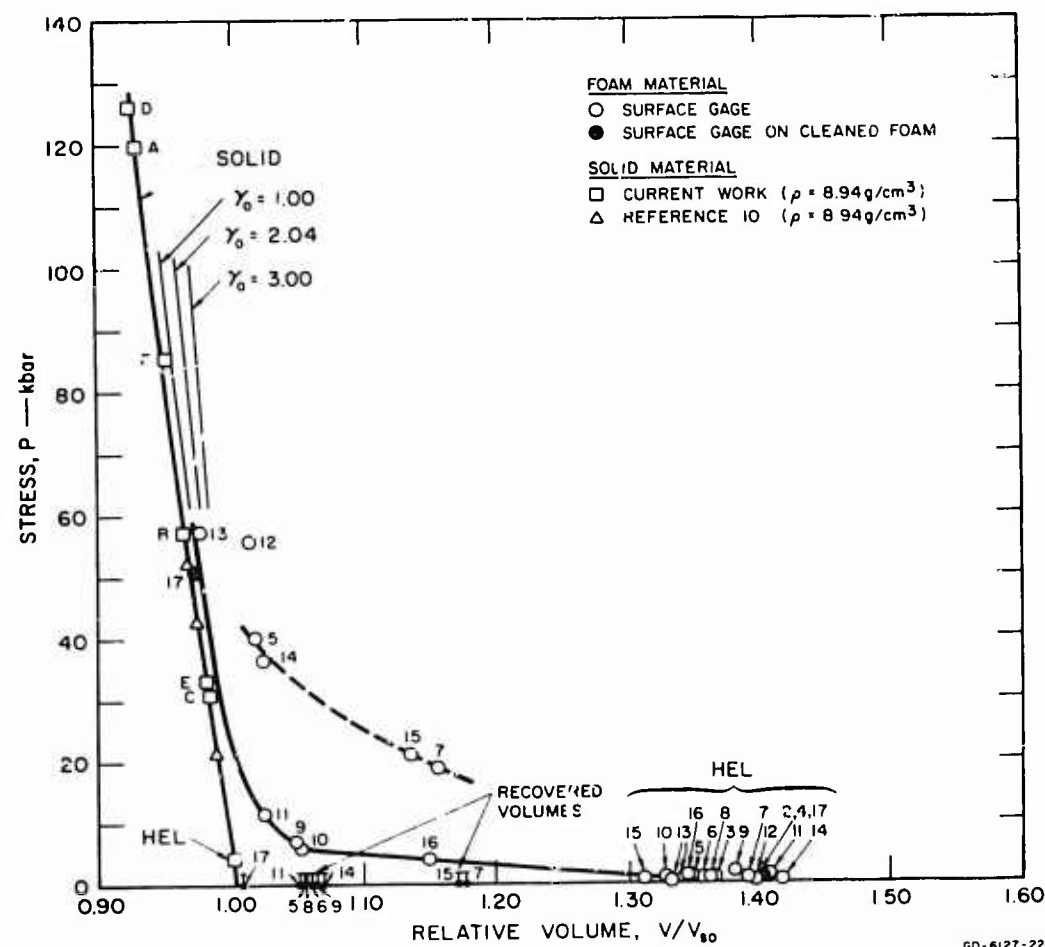


FIG. 24 STRESS-VOLUME HUGONIOT FOR COPPER

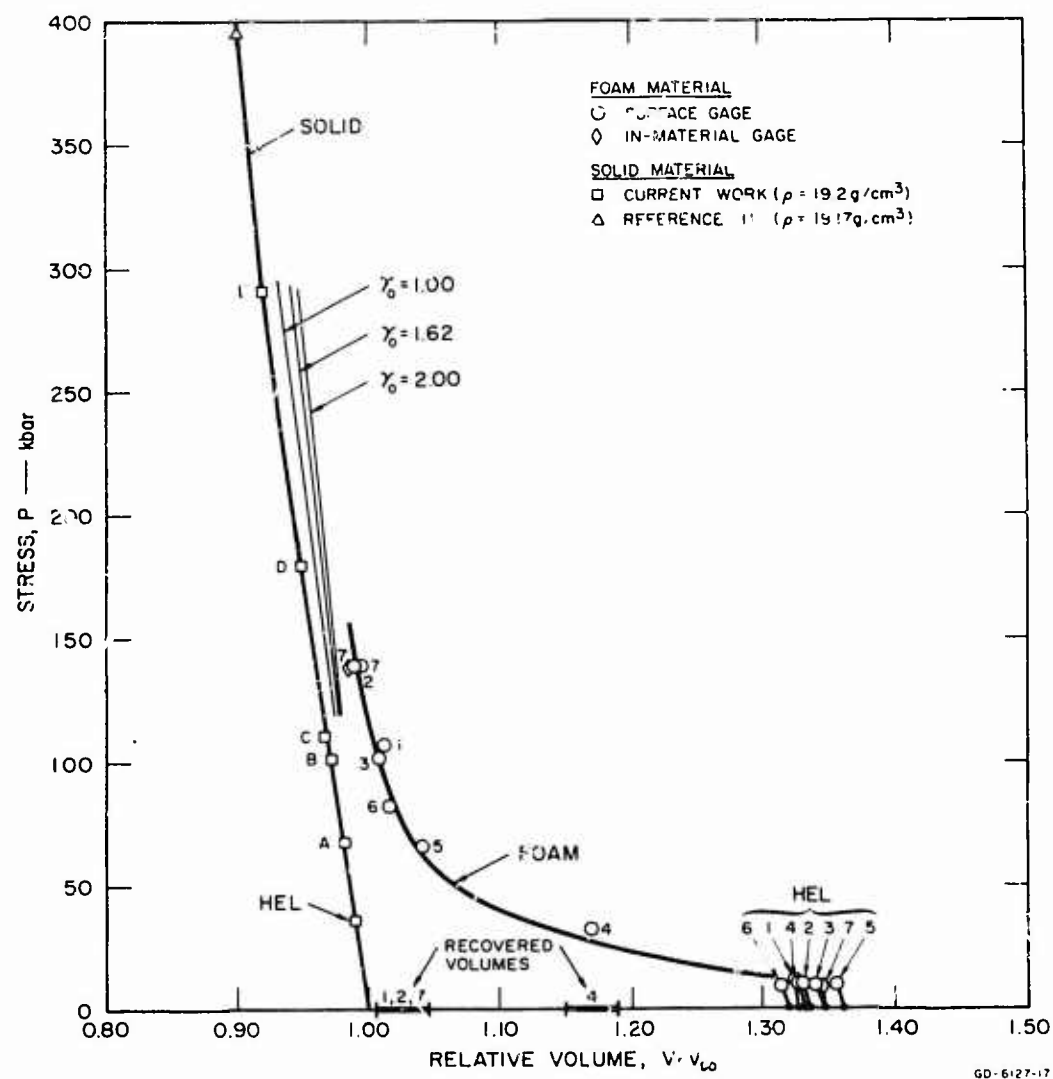


FIG. 25 STRESS-VOLUME HUGONIOT FOR TUNGSTEN

Table VI

SHOT DESIGNATIONS USED IN FIGURES

Iron	Copper	Tungsten
<u>Solid</u>		
A-12566	A-12337	A-13051
B-12570	B-12338	B-13001
C-12572	C-12573	C-13043
	D-12643	D-13049
	E-12664	E-12996
	F-13065	
<u>Foam</u>		
1-12646	1-12340	1-12994
2-12662	2-12388	2-12995
3-12663	3-12389	3-13000
4-12671	4-12424	4-13050
5-12672	5-12567	5-13052
6-12851	6-12568	6-13059
7-12906	7-12569	7-13116
8-13970	8-12571	
9-12985	9-12574	
10-13128 (clean)	10-12644	
11-13130 (clean)	11-12645	
	12-12986	
	13-12991	
	14-13056	
	15-13057	
	16-13058	
	17-13230 (clean)	

may be contrasted with the behavior above a few kilobars of aluminum and graphite of roughly the same porosity (Reference 4).

3. Interpretation of Results

a. Temperature Effects

A general model of material behavior should include the effect of heating in the foam (associated with the large amount of energy dissipation which makes foams good countermeasure materials). One would not expect that a uniform distribution is achieved in the time scale of the shock measurements. If one nevertheless implicitly assumes thermal equilibrium in addition to stress equilibrium behind the shock, reasonable agreement with experiments at high pressure can be obtained (e.g., see Reference 12). For the equilibrium case, we can apply a Mie-Grüneisen equation of state:

$$P_F - P_S = \frac{\gamma}{V} (E_F - E_S) \quad (2)$$

where the subscripts F and S refer to states along the foam Hugoniot and the solid Hugoniot, respectively. When Eq. (2) is combined with the conservation-of-energy relation across a shock front:

$$E - E_o = \frac{1}{2} P(V_o - V) \quad (3)$$

we get (after compaction, and neglecting initial surface energy of the foam particles)

$$P_F = P_{oF} + \frac{P_S \left[1 - \frac{1}{2} \frac{\gamma}{V} (V_S - V) \right]}{\left[1 - \frac{1}{2} \frac{\gamma}{V} (V_F - V) \right]} \quad (4)$$

where the subscript o refers to the precursor state in the foam or the initial state in the solid. It is found in practice that the quantity γ/V is essentially constant over a wide range of conditions, so that even if γ is not known precisely as a function of V, Eq. (4) can be reasonably well evaluated as long as γ_o is

known. This procedure has been adopted, and the values $\gamma_0 = 2.04$ (Reference 13), 1.60 (Reference 14), and 1.62 (Reference 14) have been used for copper, iron, and tungsten, respectively. Curves computed using somewhat different values of γ_0 have been included in Figures 23 to 25 for easy estimation of sensitivity to errors in γ .

It may be seen from Figures 23 through 25 that, in contrast with the results for aluminum and graphite over the porosity and stress range studied previously (Reference 4), significant heating effects are predicted for the conditions of the present experiments. Some of the experimental data are in agreement with the predictions. Even more striking is the result that substantial offsets from the predicted Hugoniot exist at stresses considerably above the dynamic "elastic" limits.*

b. Effects of Inclusions in Pores

In this connection, the relative specific volumes of recovered specimens, V/V_{S0} , where V_{S0} is the solid volume at zero stress, provide useful comparisons with the experimental Hugoniot data. On the copper Hugoniot plot (Figure 24), Shots 7 and 15 exhibit large deviations from the rest of the data. When one considers the postshot data from these experiments it becomes obvious that both the static and dynamic data show a compaction considerably less than expected for the impact conditions achieved. A similar comparison can be made for many of the foam iron data. The volumes during shock compression and the residual specific volumes of most of the specimens subjected to high shock stresses were systematically greater than the specific volumes of initially solid materials by about 10 percent for iron, 6 percent or more for copper, and 3 percent for tungsten.

*When a load is applied to a porous material, high stress concentrations exist at contact points of the particles. Thus, even the elastic precursor will in general cause a small amount of localized plastic flow which enlarges contact surfaces and relieves the high stress concentrations.

As discussed in Section II, the results of carbon oxidation analysis suggested that significant amounts of organic material may have been in the pores of the iron foam and some of the copper foam.

In an attempt to vaporize any residual solvents and other organic materials* and to remove any residual oxides in the iron foam, samples were heated in a dry H_2 atmosphere. The temperature was increased at the rate of $200^\circ F$ per hour to $1100^\circ F$. After 1 hour at $1100^\circ F$ the samples were allowed to cool slowly to room temperature in the H_2 atmosphere. This cycle was successful in producing "clean" material.

Dynamic experiments (Hugoniot points 10 and 11 of Figure 23) were performed on two cleaned iron foam specimens. Compactions which are in good agreement with theoretical predictions were achieved in these experiments. A solid line has been drawn through the Hugoniot data believed to be most representative of uncontaminated foam. It may also be noted that although the peak crushing stress was not very high in Shot 10, the postshot data show a greater residual compaction than earlier shots on "as-received" specimens which had experienced even higher stress environments.

In the case of copper foam, considerable scatter in Hugoniot data and postshot volumes was observed (see Figure 24). Similarly, the carbon oxidation analysis (Table II) disclosed that the carbon content of different specimens ranged over more than an order of magnitude. A search of processes that could introduce widely varying amounts of materials in the pores revealed that some of the specimens had been contaminated with press oil during their manufacture. This could also be responsible for the unusually large range of initial densities measured in the copper material. Hugoniot point 17 (Figure 24) and its corresponding postshot data are in agreement with the data from several other specimens, and indicate that the response of "clean" copper foam is in good agreement with theoretical predictions.

* For example, the manufacturer used a corrosion inhibitor, dicyclohexylammonium nitrite (Reference 15), in packaging the specimens.

The tungsten foam exhibits considerable strength and is not fully crushed even at 150 kbar (see Figure 25). The material analyses showed that only trace impurities existed in the tungsten specimens; they would not be detectable in the Hugoniot plots for this relatively incompressible foam. The foam tungsten data include a point labeled 7, which corresponded to a shot that had an in-material transducer in addition to the normal manganin in C-7 epoxy gage. The in-material gage measures stress directly and provides a Hugoniot point without the need for shock velocity measurements. The good agreement between results obtained by the two techniques (see Figure 25) provides strong verification of the experimental results obtained by the reverberation analysis technique.

c. Release Paths

In order to calculate shock attenuation in foams, it is essential to know the release path that the material follows as the stress is reduced by rarefactions. Release states were measured by means of manganin gages in C-7 epoxy and were also inferred from postshot measurements of residual specific volumes. Both types of data are of lower precision than the Hugoniot data. Since the shock impedance of C-7 epoxy is rather low, small errors in measured C-7 pressure produce larger errors in estimated cross-curves for materials of relatively high impedance. The postshot data, on the other hand, do not give a direct measurement of initial release path because of the long time lapse before measurements can be made. If one neglects thermal effects (which should not be large under conditions of the present study) the postshot volume can be considered an upper bound on the zero pressure terminus of the release curve, and can be used to corroborate and interpret release curve data obtained from C-7 pressure measurements. It must be borne in mind, however, that when quartz gages were used, reflected shocks were sent into the specimens, so that release occurred from a state of higher stress than the measured Hugoniot state.

For the materials studied in the current work, the dynamic and post-shot data (Figures 23, 24, and 25) defined release paths roughly parallel to

the Hugoniot of the solid matrix material. Foam iron that had not been cleaned exhibited the maximum opening up of pores, with postshock volumes roughly from 2 to 5 percent greater than would be attained by release paths parallel to that of initially solid material. Stress-particle velocity Hugoniot and release curves are shown in Figures 26, 27, and 28 for iron, copper, and tungsten. The cross-curve points are located on the C-7 curve. The Hugoniot elastic limits, HEL, plotted for both solids and foams, are average values.

Some scatter of the foam Hugoniot data is apparent in these plots. This behavior is expected when there is no attempt to normalize the points to a unique initial density. A dashed curve has been fit to the data to provide a reference basis. In Figure 26 the data on the clean iron foam shots (8 and 11) are connected by a solid curve which should be more representative of the behavior of the foam matrix material without inclusions.

The slash marks on the C-7 Hugoniot correspond to the release paths the shocked (initially porous) metal would follow if temperature rises are neglected and if it behaves exactly like a nonporous solid after shock.

These results for contaminated foams point to the fact that foams whose pores are filled or partially filled with a relatively compressible material may be effective countermeasure materials in situations where preshocking would collapse a clean foam and render it ineffective. Such composite foams might also be designed to subsequently slowly "open up" to provide protection for subsequent hits (i.e., provide a restrictive defense).

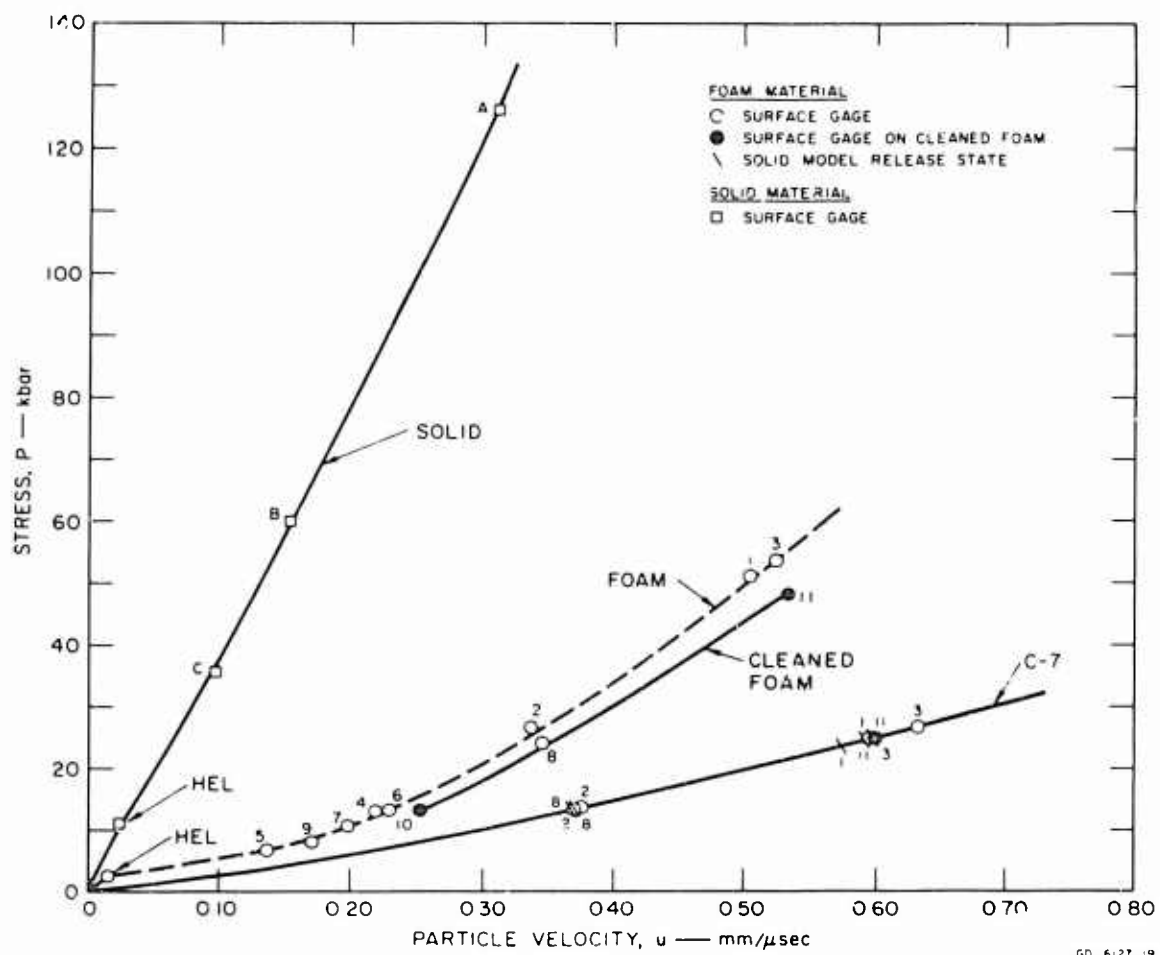


FIG. 26 STRESS-PARTICLE VELOCITY HUGONIOT AND RELEASE CURVES FOR IRON

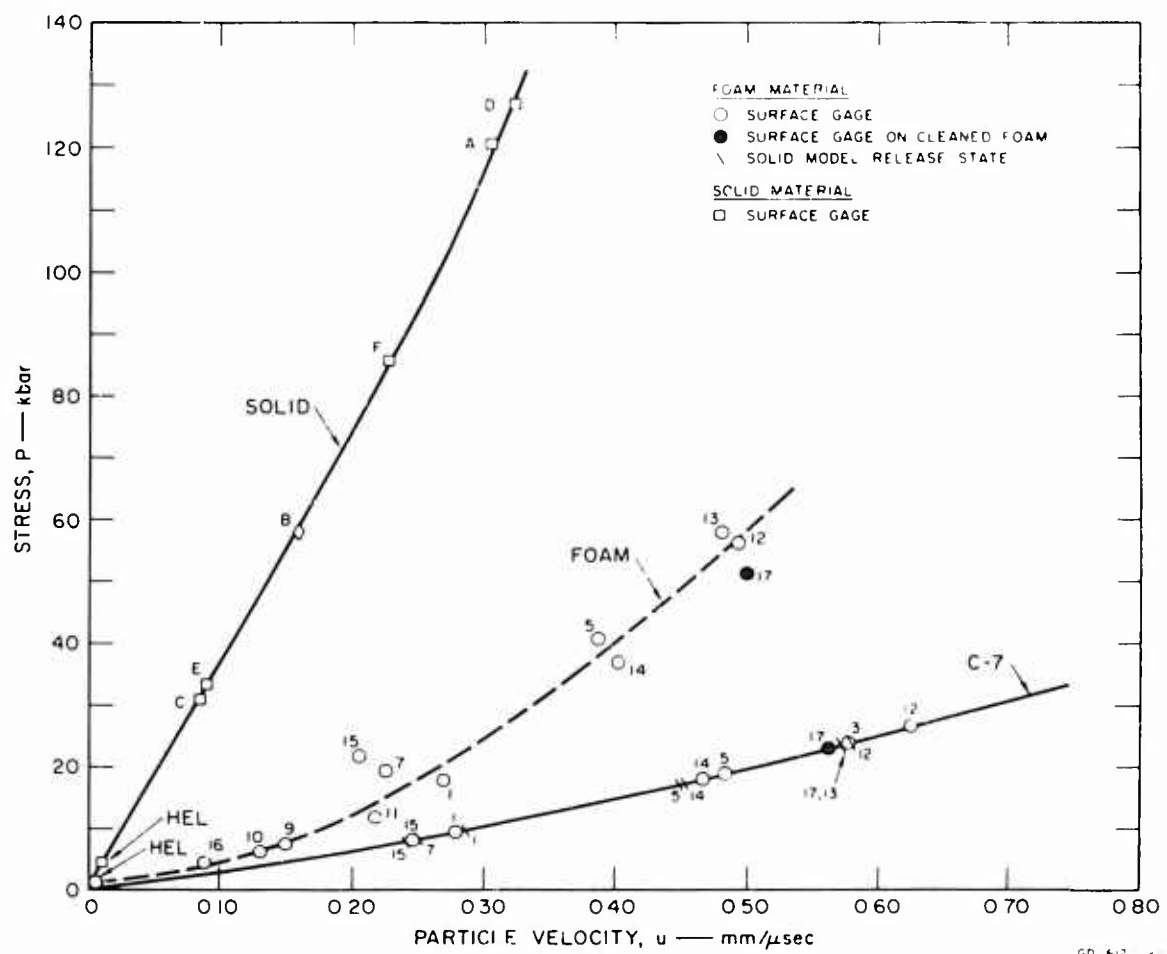


FIG. 27 STRESS-PARTICLE VELOCITY HUGONIOT AND RELEASE CURVES FOR COPPER

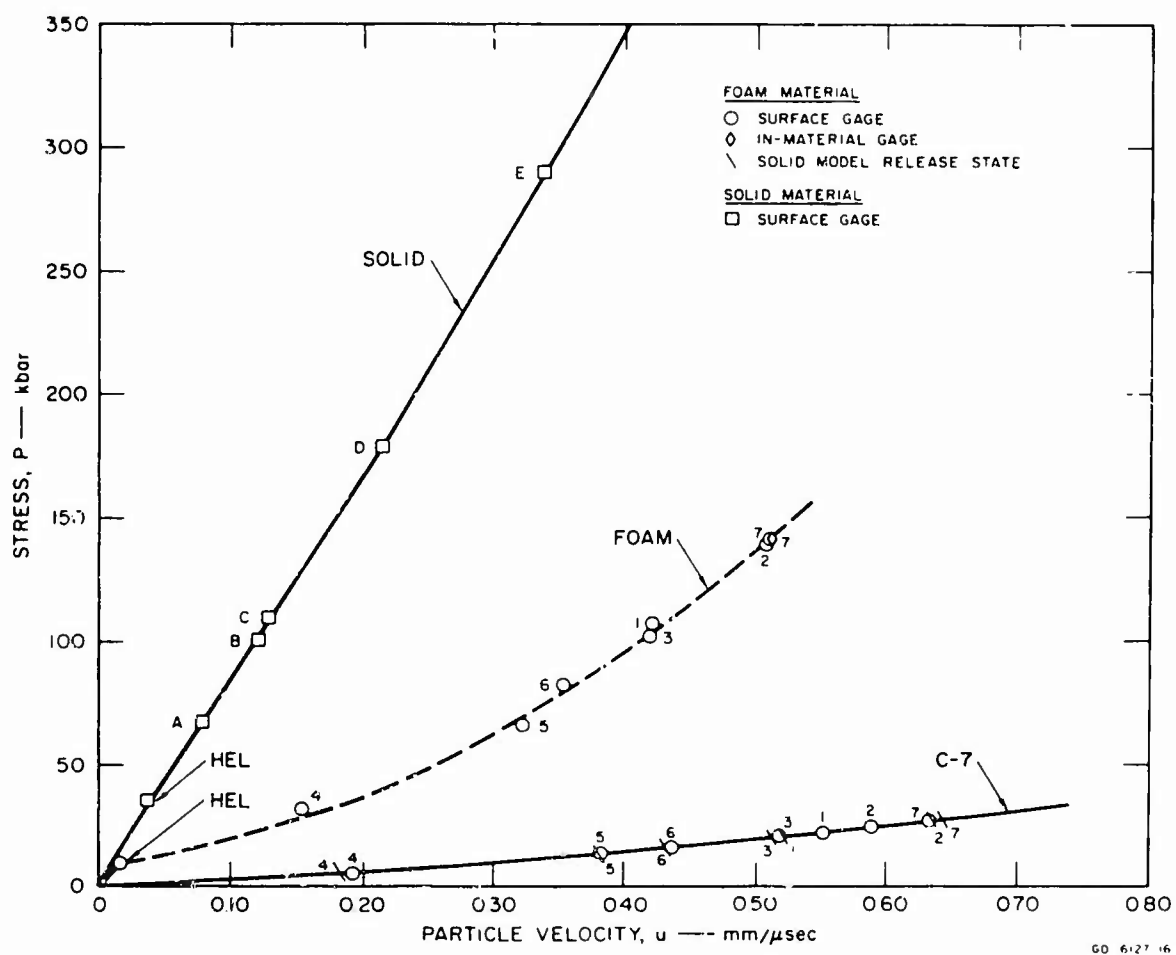


FIG. 28 STRESS-PARTICLE VELOCITY HUGONIOT AND RELEASE CURVES FOR TUNGSTEN

SECTION VI

SUMMARY AND RECOMMENDATIONS

In order to predict shock wave propagation and attenuation in a material, it is first necessary to obtain Hugoniot and release adiabat measurements for the material. When the material is initially porous, the Hugoniot may display significant temperature effects even at relatively low stresses (e.g., below 100 kbar), and release adiabats may deviate substantially from the Hugoniot curves.

Manganin and quartz gage techniques were employed to obtain Hugoniot and release state measurements up to 56 kbar for porous copper (71-76% of crystal density) 52 kbar for porous iron (68-72% of crystal density), and 140 kbar for porous tungsten (73-76% of crystal density). Inclusions in the pores substantially altered the compaction behavior of copper and iron foams, but above about 20 kbar "clean" specimens of these porous materials will compact to the volumes predicted by a Mie-Grüneisen equation of state. Tungsten foam exhibited substantial residual crushing strength up to at least 140 kbar, and was thus never fully compacted under conditions of the experiments.

Precursor amplitudes were 1.1, 2.5, and 9.6 kbar for the copper, iron, and tungsten foams, respectively, and all foam materials displayed release curves similar to those for initially solid material, even when the foams were not fully compacted. Hugoniot data were obtained for solid copper and iron up to about 130 kbar, for solid tungsten up to 290 kbar, and for C-7 epoxy up to 28 kbar.

The present contract is closely coordinated with Contract No. F29601-67-C-0073, under which computations based on theoretical or semi-empirical models of material behavior are being developed. Most recommendations for further work must await the conclusion of work under that contract; however, it is already clear that the following are worthy of further attention:

1. Foams whose pores are filled or partially filled with some relatively compressible material are not only of interest in understanding composite materials, but may have major importance in allowing foams to operate effectively as countermeasure materials in "shine-through" situations where premature collapse of the foams would render them ineffective.

2. Structural variables such as particle strength, size, and shape, bond strength, and amount of porosity should be investigated as to their effect on precursor speed and amplitude and on the Hugoniot and release curves at low stresses. This will lead to optimization of foam parameters.

3. Spall behavior of initially porous materials should be studied in terms of the behavior of initially solid materials of the same composition.

4. In-material gages have been made to operate successfully in porous materials and promise to be an extremely valuable tool for studying material response to shock loading. Further experimental work needs to be done, however, to establish more general design criteria.

5. Metal foams with filled or partially filled pores designed to recover initial dimensions slowly after receiving a hit should be investigated in terms of providing a restrike defense capability. Similar behavior was observed earlier in "clean" porous graphite.

Possible correlations between dynamic and quasi-static behavior of foams are currently being explored under Contract No. F29601-67-C-0073.

APPENDIX
SUMMARY OF STATIC AND DYNAMIC DATA

Table VII
INITIAL CONDITIONS FOR DYNAMIC EXPERIMENTS
ON SOLID AND FOAM IRON

Shot Number	Specimen Thickness (mm)	Projectile Velocity (mm/ μ sec)	Max. Tilt across Gage (μ sec)	Measured Longitud. Acoustic Velocity (mm/ μ sec)	Measured Density (g/cm ³)	Specimen Number
<u>Solid</u>				5.96 ^a	7.81 ^a	
12566M ^b	6.40	0.621	<0.010			Fe4S
12570M	6.42	0.303	<0.010			Fe5S
12572Q ^b	6.41	0.185	0.032			Fe3S
<u>Foam</u>						
12646M	4.57	0.633	0.022	3.32	5.58	Fe4C
12662M	4.05	0.402	0.035	3.28	5.58	Fe6C
12663M	2.75	0.658	0.012	3.39	5.58	Fe7B
12671Q	2.64	0.254	0.030	3.29	5.58	Fe1B
12672Q	2.64	0.151	0.042	3.28	5.56	Fe8B
12851Q	2.72	\approx 0.26	0.010	--	--	Fe15B
12906Q	2.79	0.222	0.017	3.32	5.63	Fe2B
12970M	2.89	0.405	<0.010	3.23	5.42	Fe4B
12985Q	2.88	0.188	0.064	3.20	5.55	Fe9B
13128Q	3.44	0.283	0.028	3.0	5.50	Fe4D
13130M	5.92	0.648	0.015	2.8	5.33	Fe1D

^a Average values for solids.

^b M = manganin in C-7 epoxy transducer.
Q = quartz gages in C-7 epoxy loaded with glass beads.

Table VIII

PRECURSOR (WAVE 1) DATA FROM DYNAMIC EXPERIMENTS
ON SOLID AND FOAM IRON

Shot Number	Measured			Calculated		
	Peak Trans- ducer Stress ^a (kbar)	First- Motion Velocity $0U_1$ (mm/ μ sec)	Half-Wave Velocity $1/2U_1$ (mm/ μ sec)	Particle Velocity u (mm/ μ sec)	Peak Stress P (kbar)	Relative Volume (V/V_{so}) ^b
<u>Solid</u>						
12566	1.4M	6.06	5.74	0.026	11.5	0.996
12570	1.6M	6.14	5.74	0.028	12.7	0.995
12572	4.6Q	$\approx 6.$	≈ 5.5	≈ 0.02	≈ 9.1	≈ 0.99
<u>Foam</u>						
12646	0.7M	3.43	3.30	0.012	2.2	1.394
12662	0.6M	3.26	3.01	0.012	1.9	1.395
12663	-- M	3.53	3.49	≈ 0.02	$\approx 3.$	≈ 1.4
12671	3.4Q	3.44	3.36	0.021	3.9	1.391
12672	2.6Q	3.00	2.61	0.018	2.6	1.390
12851	-- Q	3.44	3.24	≈ 0.02	$\approx 3.$	≈ 1.4
12906	-- Q	3.18	3.11	≈ 0.02	$\approx 3.$	≈ 1.4
12970	0.9M	3.43	3.30	0.016	2.8	1.435
12985	1.7Q	3.13	2.83	0.011	1.8	1.401
13128	1.9Q	3.28	3.05	0.012	2.1	1.416
13130	0.5M	2.79	2.73	0.014	2.0	1.457

^a M = manganin in C-7 epoxy transducer. Q = quartz gage.

^b Using $V_{so} = 0.1280 \text{ cm}^3/\text{g}.$

Table IX

SHOCK (WAVE 2) DATA FROM DYNAMIC EXPERIMENTS
ON SOLID AND FOAM IRON

Shot Number	Measured			Calculated		
	Peak Trans- ducer Stress ^a (kbar)	Half-Wave Velocity $1/2 U_2$ (mm/ μ sec)	Reverber- ation ^b Time Δt (μ sec)	Particle Velocity u (mm/ μ sec)	Peak Stress P (kbar)	Relative Volume (V/V_{so}) ^c
<u>Solid</u>						
12566	23.1M	5.18	0.10	0.309	126.2	0.941
12570	9.4M	4.90	0.15	0.152	60.0	0.970
12572	19.3Q	4.56	0.16	0.096	35.6	0.980
<u>Foam</u>						
12646	24.9M	1.78	0.74	0.504	51.1	1.006
12662	13.8M	1.37	0.95	0.336	26.6	1.064
12663	24.9M	1.80	0.49	0.523	53.6	0.997
12671	15.4Q	0.84	--	≈ 0.22	$\approx 13.$	≈ 1.05
12672	-- Q	0.67	--	≈ 0.14	$\approx 7.$	≈ 1.14
12851	> 14. Q	0.88	--	≈ 0.23	$\approx 13.$	≈ 1.06
12906	> 6. Q	0.77	--	≈ 0.20	$\approx 11.$	≈ 1.05
12970	13.4M	1.21	0.78	≈ 0.345	≈ 24.2	≈ 1.039
12985	6.1Q	0.70	--	≈ 0.17	$\approx 8.$	≈ 1.08
13128	21. Q	0.85	--	≈ 0.25	$\approx 13.$	≈ 1.01
13130	-- M	1.60	1.09	0.532	46.2	0.982

^a M = manganin in C-7 epoxy transducer. Q = quartz gage.

^b Time between arrival of Wave 1 and the first reverberation at the target-gage interface. When no reverberation time was available for foam specimens with manganin in C-7 gages, the calculated data for Wave 2 are less reliable and have not been included in the Hugoniot plots. The shock impedance of quartz is close to that of the foam precursor, so this comment does not apply for quartz gages.

^c Using $V_{so} = 0.1280 \text{ cm}^3/\text{g}$.

Table X
INITIAL CONDITIONS FOR DYNAMIC EXPERIMENTS
ON SOLID AND FOAM COPPER

Shot Number	Specimen Thickness (mm)	Projectile Velocity (mm/ μ sec)	Max. Tilt across Gage (μ sec)	Measured Longitud. Acoustic Velocity (mm/ μ sec)	Measured Density (g/cm ³)	Specimen Number
<u>Solid</u>				4.98 ^a	8.94 ^a	
12337M ^b	9.43	0.607	0.024			Cu1S
12338M ^c	9.33	0.315	0.019			Cu2S
12664Q ^b	6.31	0.181	0.033			Cu5S
12643Q	6.39	0.639	<0.010			Cu4S
12573Q	6.32	0.170	0.027			Cu3S
13065M	6.36	0.448	0.014			Cu15S
13048M	3.09	0.475	--			Cu14S
<u>Foam</u>						
12339M	2.95	0.558	--	--	~6.6	Cu1F
12340M	3.03	0.317	0.014	--	~6.6	Cu2F
12388M	2.84	0.461	0.013	--	6.37	Cu5F
12389M	2.91	0.614	--	--	6.49	Cu4F
12424 ^d	2.61	0.607	--	--	6.37	Cu6F
12567M	3.94	0.498	<0.010	3.18	6.62	Cu2C
12568M	4.34	0.641	--	3.18	6.58	Cu1C
12569M	2.70	0.278	<0.010	3.18	6.42	Cu7A
12571M	4.36	0.641	0.015	3.20	6.56	Cu4C
12574Q	2.83	0.170	0.032	3.24	6.45	Cu15A
12644Q	1.67	0.146	0.090	3.20	6.72	Cu13A
12645Q	2.63	0.249	0.016	3.20	6.34	Cu14A
12986M	2.86	0.643	0.018	3.03	6.40	Cu6A
12991M	4.52	0.635	0.015	3.18	6.56	Cu1J
13056M	3.23	0.503	0.019	2.90	6.31	Cu3C
13057M	1.78	0.265	0.011	2.82	6.82	Cu4D
13058Q	1.50	0.098	0.028	3.01	6.64	Cu3D
13230M	3.90	0.637	0.023	2.8	6.36	Cu3J

^a Measured nominal value for solid copper.

^b M = manganin in C-7 epoxy transducer, surface-mounted.
Q = quartz gage in C-7 epoxy loaded with glass beads.

^c In-material gage (see text).

^d Streak-camera free-surface measurement.

Table XI
PRECURSOR (WAVE 1) DATA FROM DYNAMIC EXPERIMENTS
ON SOLID AND FOAM COPPER

Shot Number	Measured			Calculated		
	Peak Transducer Stress ^a (kbar)	First-Motion Velocity $0U_1$ (mm/ μ sec)	Half-Wave Velocity $1/2U_1$ (mm/ μ sec)	Particle Velocity u (mm/ μ sec)	Peak Stress P (kbar)	Relative Volume $(V/V_{so})^b$
<u>Solid</u>						
12337	-- M	4.82	--	0.008	3.2	0.999
12338	5.4 ^c	4.61	4.23	0.015	5.7	0.997
12664	2.2Q	4.86	4.61	0.010	4.3	0.998
12643	-- Q	--	--	--	--	--
12573	3.5Q	4.63	4.48	0.010	4.2	0.998
13065	0.4M	4.81	4.68	0.008	3.2	0.999
13048	-- M	--	--	--	--	--
<u>Foam</u>						
12339	-- M ^d	--	--	--	--	--
12340	$\approx 0.4M$	$\approx 2.$	$\approx 2.$	≈ 0.01	$\approx 1.$	≈ 1.34
12388	-- M ^e	--	--	--	--	--
12389	-- M ^e	3.06	2.83	--	--	--
12424	f	--	--	--	--	--
12567	0.3M	3.13	2.80	0.007	1.4	1.346
12568	-- M ^e	--	--	--	--	--
12569	$\approx 0.4M$	≈ 2.6	≈ 2.6	≈ 0.008	≈ 1.2	≈ 1.39
12571	0.3M	≈ 2.7	≈ 2.7	≈ 0.006	≈ 1.1	≈ 1.36
12574	1.7Q	3.14	3.00	≈ 0.010	2.0	1.381
12644	1.3Q	$\approx 2.$	$\approx 2.$	≈ 0.009	$\approx 1.$	≈ 1.32
12645	1.3Q	3.48	2.90	0.008	1.5	1.407
12986	0.2M	3.05	2.93	0.004	0.7	1.396
12991	0.1M	3.33	3.23	0.002	0.6	1.331
13056	0.2M	3.34	3.09	0.004	0.8	1.416
13057	0.2M	3.30	3.03	0.005	1.0	1.310
13058	1.3Q	≈ 2.7	≈ 2.4	≈ 0.009	≈ 1.4	≈ 1.34
13230	0.2M	2.95	2.81	0.004	0.8	1.405

^a Unless otherwise noted, M = manganin in C-7 epoxy, Q = quartz gage.

^b Using $V_{so} = 0.1119 \text{ cm}^3/\text{g}$.

^c Manganin in copper.

^d No dynamic stress data were recorded for this shot.

^e Average stress value used with actual specimen density and precursor velocity to calculate precursor state.

^f Optical free-surface measurement.

Table XII

SHOCK (WAVE 2) DATA FROM DYNAMIC EXPERIMENTS
ON SOLID AND FOAM COPPER

Shot Number	Measured			Calculated ^a		
	Peak Trans- ducer Stress ^b (kbar)	Half-Wave Velocity $1/2 U_2$ (mm/ μ sec)	Reverber- ation Time ^c Δt (μ sec)	Particle Velocity u (mm/ μ sec)	Peak Stress P (kbar)	Relative Volume (V/V_{so}) ^d
Solid						
12337	23.1M	<4.4	--	>0.30	<120	~ 0.931
12338	-- M	<4.1	--	>0.16	<58	~ 0.962
12664	16.9Q	4.13	--	0.089	33.2	0.979
12643	>20. Q	4.38	--	0.324	126.8	0.927
12573	21.2Q	4.06	--	0.084	30.9	0.980
13065	14.7M	4.28	--	0.224	85.9	0.948
13048	-- M	--	--	--	--	--
Foam						
12339	-- M	--	--	--	--	--
12340	9.4M	0.98	--	≈ 0	$\approx 18.$	(≈ 0.98)
12388	15.3M	1.51	--	(≈ 0.48)	($\approx 35.$)	(≈ 1.07)
12389	23.8M	1.62	--	(≈ 0.48)	($\approx 50.$)	(≈ 0.98)
12424	--	1.29	--	(≈ 0.49)	($\approx 41.$)	(≈ 0.87)
12567	18.9M	1.56	0.66	0.387	40.4	1.016
12568	23.2M	1.69	--	(≈ 0.49)	($\approx 55.$)	(≈ 0.97)
12569	8.5M	1.29	0.66	0.224	19.1	1.155
12571	23.2M	1.65	0.76	(0.50)	(54.)	(0.96)
12574	8.9Q	0.59	--	≈ 0.15	$\approx 7.$	≈ 1.05
12644	10.7Q	0.59	--	≈ 0.13	$\approx 6.$	≈ 1.05
12645	22.2Q	0.77	--	≈ 0.22	$\approx 12.$	≈ 1.02
12986	26.6M	1.78	0.47	0.491	56.1	1.013
12991	$\approx 24.$ M	1.78	0.79	0.479	57.6	0.975
13056	18.0M	1.43	0.75	0.401	36.6	1.023
13057	8.0M	1.50	0.35	0.205	21.4	1.134
13058	4.8Q	0.55	--	≈ 0.09	$\approx 4.$	≈ 1.15
13230	23.1M	1.60	0.75	0.498	51.0	0.971

^a Data in parentheses were less reliable and were therefore not used for plotting Hugoniot or release states.

^b M = manganin in C-7 epoxy transducer. Q = quartz gage.

^c Time between arrival of Wave 1 and the first reverberation at the target-gage interface. (See Note b, Table IX.)

^d Using $V_{so} = 0.1119 \text{ cm}^3/\text{g}$.

Table XIII

INITIAL CONDITIONS FOR DYNAMIC EXPERIMENTS
ON SOLID AND FOAM TUNGSTEN^a

Shot Number	Specimen Thickness (mm)	Projectile Velocity (mm/ μ sec)	Max. Tilt across Gage (μ sec)	Measured Longitud. Acoustic Velocity (mm/ μ sec)	Measured Density (g/cm ³)	Specimen Number
<u>Solid</u>				5.40 ^b	19.2	
12996	3.29	0.675	0.014			WS2E
13001	3.30	0.245	0.026			WS1E
13043	6.48	0.264	0.011			WS4C
13049	6.15	0.428	0.011			WS2C
13051	6.46	0.161	0.079			WS5C
<u>Foam</u>						
12994	3.06	0.553	0.030	3.53	14.3	WF24
12995	3.10	0.676	0.022	3.69	14.2	WF25
13006	2.16	0.544	0.039	3.60	14.2	WF12
13050	1.19	0.193	0.015	3.73	14.4	WF18
13052	2.04	0.405	0.025	3.60	14.1	WF16
13059	2.15	0.456	0.031	3.59	14.5	WF13
13116 ^c	1.16	0.677	0.025	3.83	14.2	WF19

^a Except for Shot 13116, all tungsten shots used a standard manganin in C-7 epoxy pressure transducer.

^b Average value for solid.

^c Three-gage shot including two standard manganin in C-7 gages and one gage in tungsten.

Table XIV

PRECURSOR (WAVE 1) DATA FROM DYNAMIC EXPERIMENTS
ON SOLID AND FOAM TUNGSTEN^a

Shot Number	Measured			Calculated		
	Peak Trans- ducer Stress (kbar)	First- Motion Velocity U_1 (mm/ μ sec)	Half-Wave Velocity $1/2 U_1$ (mm/ μ sec)	Particle Velocity u (mm/ μ sec)	Peak Stress P (kbar)	Relative Volume (V/V_{SO}) ^b
<u>Solid</u>						
12996	--	--	--	--	--	--
13001	2.3	5.30	4.77	0.039	36.1	0.990
13043	2.3	5.13	4.87	0.039	36.3	0.990
13049	2.2	5.04	4.91	0.037	35.2	0.991
13051	2.2	5.11	4.83	0.038	35.5	0.991
<u>Foam</u>						
12994	1.0	4.20	4.10	0.019	11.2	1.334
12995	1.0	3.91	3.74	0.018	9.8	1.341
13000	1.1	3.68	3.51	0.020	9.8	1.341
13050	1.0	4.01	3.71	0.019	10.0	1.326
13052	1.0	4.10	3.73	0.018	9.6	1.357
13059	0.9	3.77	3.61	0.017	8.8	1.314
13116 ^c	0.8	4.3	3.74	0.016	8.3	1.344

^a Except for Shot 13116, all tungsten shots used a standard manganin in C-7 epoxy pressure transducer.

^b Using $V_{SO} = 0.05208 \text{ cm}^3/\text{g}$.

^c In material gage used in addition to the standard manganin in C-7 Type.

Table XV

SHOCK (WAVE 2) DATA FROM DYNAMIC EXPERIMENTS
ON SOLID AND FOAM TUNGSTEN

Shot Number	Measured			Calculated		
	Peak Trans- ducer Stress ^a (kbar)	Half-Wave Velocity $1/2 U_2$ (mm/sec)	Reverber- ation Time ^b Δt^c (μ sec)	Particle Velocity u (mm/ μ sec)	Peak Stress P (kbar)	Relative Volume $(V/V_{so})^c$
<u>Solid</u>						
12996	27.9	4.41		0.338	289.5	0.923
13001	8.2	4.15		0.121	101.0	0.971
13043	8.1	4.24		0.129	109.8	0.969
13049	14.9	4.25		0.213	173.9	0.950
13051	3.5	4.27		0.077	67.4	0.982
<u>Foam</u>						
12994	22.7	1.68	0.60	0.421	107.2	1.012
12995	25.	1.88	0.52	0.506	139.3	0.988
13000	20.6	1.63	0.43	0.419	101.9	1.009
13050	6.1	1.15	0.30	0.153	31.9	1.169
13052	13.8	1.33	0.48	0.323	66.0	1.042
13059	16.5	1.51	0.46	0.354	82.2	1.017
13116	27.5	1.93	0.16	0.505	141.9	1.001
13116 ^d	139	--	--	0.513	--	0.984

^a Except for Shot 13116, all tungsten shots used a standard manganin in C-7 epoxy pressure transducer.

^b Time between arrival of Wave 1 and the first reverberation at the target-gage interface. (See Note b, Table IX.)

^c Using $V_{so} = 0.05208 \text{ cm}^3/\text{g}$. (See Note c, Table A-3.)

^d Analyzed using the final stress measurement of the in-material gage.

This page left intentionally blank.

REFERENCES

1. Fowles, G. R. and Curran, D. R.; (U) Experimental Testing of Shock-Attenuating Materials, AFSWC-TDR-62-22 [AF 29(601)-4363], AF Special Weapons Center, Kirtland AFB, NM, March 1962. (Secret-RD)
2. Rempel, J.R.; Shock Wave Attenuation in Elastic-Rigid Foams, AFWL-RTD-TDR-63-3056, [AF 29(601)-4363], AF Weapons Laboratory, Kirtland AFB, NM, August 1, 1963.
3. Rempel, J. R., Erkman, J. O., Schmidt, D. N. and Isbell, W. M.; Shock Attenuation in Solid and Distended Materials, AFWL-TR-64-119, [AF 29(601)-6040], AF Weapons Laboratory, Kirtland AFB, NM, February 1966.
4. Linde, R. K. and Schmidt, D. N.; Attenuation of Shock Waves in Distended Materials, AFWL-TR-66-13, [AF 29(601)-6734], December 23, 1965.
5. Materials Engineering 66, 5, p. 30 (1967).
6. Properties and Selection of Metals, Vol. 1 of Metals Handbook, T. Lyman, ed., 8th Edition, American Society for Metals, Metals Park, Ohio, 1961.
7. Keough, D.D.; Pressure Transducer for Measuring Shock Wave Profiles. Phase IX: Additional Gage Development, DASA 1414-1 (DA-49-146-XZ-096), (AD 459 058), Defense Atomic Support Agency, Washington, D.C., November 1964.
8. Graham, R.A., Neilson, T.W., and Benedick, W.B.; J. Appl. Phys. 36, ITIS (1965).
9. Taylor, J. W. and Rice, M. H.; "Elastic-Plastic Properties of Iron," J. Appl. Phys. 34, 364-371 (1963).
10. Munson, D. E. and Barker, L. M.; "Dynamically Determined Pressure-Volume Relationships for Aluminum, Copper, and Lead," J. Appl. Phys. 37, 1652-1660 (1966).

11. McQueen, R. G. and Marsh, S. P.; "Equation of State for Nineteen Metallic Elements from Shock-Wave Measurements to Two Megabars," J. Appl. Phys. 31, 1253-1269 (1960).
12. Anderson, G. D. and Fahrenbruch, A.; Equation of State of Solids: II. Aluminum and Teflon, AFWL-TR-67-43, [AF 29(601)-7214], AF Weapons Laboratory, Kirtland AFB, NM, September 1967.
13. Rice, M. H., McQueen, R. G., and Walsh, J. M.; "Compression of Solids by Strong Shock Waves," Solid State Physics, Vol. 6, (F. Seitz and D. Turnbull, eds.), Academic Press Inc., New York, 1958, pp. 1-63.
14. Slater, J. C.; Introduction to Chemical Physics, McGraw-Hill, Inc., New York, 1939.
15. Wachter, A., Skei, T., and Stillman, N.; "Dicyclohexylammonium Nitrite, a Volatile Corrosion Inhibitor for Corrosion Preventive Packaging," Corrosion, 7, No. 9, 1951.

DISTRIBUTION

No. cys

HEADQUARTERS USAF

1	Hq USAF (AFTAC/TD-3, Capt Herman), Wash, DC	20330
1	USAF Dep, IG (AFIDI-AS2), Norton AFB, Calif	92409
1	USAF Dir Nuc Safety (AFINS), Kirtland AFB, NM	87117

MAJOR AIR COMMANDS

1	AFSC, Andrews AFB, Wash, DC	20331
1	(SCTSW)	
1	(SCTL)	
1	AUL(SE)-67-464, Maxwell AFB, Ala	36112
1	USAFIT-L, Bldg 640, Wright-Patterson AFB, Ohio	45433

AFSC ORGANIZATIONS

1	AFSC STLO, R & T Div, AFUPO, Los Angeles, Calif	90045
1	AFSC STLO, (SCTL-6), Ste 104, 363 Taaffe Ave, Sunnyvale, Calif	94086
1	FTD (TDBTL), Wright-Patterson AFB, Ohio	45433
1	AF Materials Lab, Wright-Patterson AFB, Ohio	45433 (MAMD, I. D. Forney, I. T. Nicholas)
1	AF Avionics Lab, Wright-Patterson AFB, Ohio	45433
1	AF Flight Dyn Lab, Wright-Patterson AFB, Ohio	45433 (MAMD, I. D. Forney, I. T. Nicholas)
1	AF Aero-Propulsion Lab, Wright-Patterson AFB, Ohio	45433
1	ASC, Wright-Patterson AFB, Ohio	45433
1	(ASAPR)	
1	(ASRCP)	
1	(ASAMC)	
1	SEG (SESGS, J. L. Wilkinson), Wright-Patterson AFB, Ohio	45433
1	ORA (RRRD), Holloman AFB, NM	88330
1	AEDC (AEYD), Arnold AFS, Tenn	37289
1	SAMSO, AFUPO, Los Angeles, Calif	90045
1	(SMSDI-IDEP)	
1	(SMT)	
1	(SMTC)	

UNCLASSIFIED

Security Classification

DOCUMENT CONTROL DATA - R & D		
<i>Security classification of title, body of abstract and indexing annotation must be entered when the overall report is classified</i>		
1. ORIGINATING ACTIVITY (Corporate author)		2a. REPORT SECURITY CLASSIFICATION
Stanford Research Institute Menlo Park, California		UNCLASSIFIED
2b. GROUP		
3. REPORT TITLE		
RESPONSE OF DISTENDED COPPER, IRON, AND TUNGSTEN TO SHOCK LOADING		
4. DESCRIPTIVE NOTES (Type of report and inclusive dates)		
23 June 1966 to 29 February 1968		
5. AUTHOR(S) (First name, middle initial, last name)		
D. N. Schmidt and R. K. Linde		
6. REPORT DATE	7a. TOTAL NO. OF PAGES	7b. NO. OF PAGES
July 1968	92	15
8a. CONTRACT OR GRANT NO.	9a. ORIGINATOR'S REPORT NUMBER(S)	
AF 29(601)-7236	AFWL-TR-68-33	
b. PROJECT NO.	9b. OTHER REPORT NO(S) (Any other numbers that may be assigned this report)	
5710	SRI PGU-6127	
c. Subtask	RAS1106	
d.		
10. DISTRIBUTION STATEMENT This document is subject to special export controls and each transmittal to foreign governments or foreign nationals may be made only with prior approval of AFWL (WLRP), Kirtland AFB, NM 87117. Distribution is limited because of the technology discussed in this report.		
11. SUPPLEMENTARY NOTES		12. SPONSORING MILITARY ACTIVITY
		AFWL (WLRP) Kirtland AFB, New Mexico 87117
13. ABSTRACT		
<p>(Distribution Limitation Statement No. 2)</p> <p>An experimental study of the dynamic response of porous (two-thirds of crystal density) copper, iron, and tungsten was performed, using manganin and quartz transducer techniques. The data acquired include measurements of Hugoniot and release states up to about 60 kbar for porous copper, 50 kbar for porous iron, and 140 kbar for porous tungsten. It was found that inclusions in the pores substantially altered the compaction behavior of porous copper and iron, but that above about 20 kbar, "clean" foams of these materials will compact to the volumes predicted by a Mie-Grüneisen equation of state. Tungsten foam exhibited substantial residual crushing strength up to at least 140 kbar, and was thus never fully compacted under the conditions of the experiments.</p> <p>Precursor amplitudes were nominally 1, 2.5, and 10 kbar for the copper, iron, and tungsten foams, respectively, and all foam materials displayed release curves similar to those for initially solid material, even when the foams were not fully compacted. Hugoniot data were obtained for solid copper and iron up to about 130 kbar, for solid tungsten up to 290 kbar, and for C-7 epoxy up to 28 kbar.</p>		

DD FORM 1473
1 NOV 64

UNCLASSIFIED

Security Classification

UNCLASSIFIED

Security Classification

14	KEY WORDS	LINK A		LINK B		LINK C	
		ROLE	WT	ROLE	WT	ROLE	WT
	Shock propagation						
	Shock attenuation						
	Hugoniot						
	Equation of state						
	Dynamic response						
	Distended materials						

AFBC (KAFB NM)

UNCLASSIFIED

Security Classification